



EVALUATION OF A LINEAR EXPRESSION FOR RETRIEVAL OF
DIRECTIONAL WAVE SPECTRA FROM COMPLEX SAR LOOK CROSS
SPECTRA

Yuri de Oliveira Brasil Corrêa

Dissertação de Mestrado apresentada ao Programa de Pós-graduação em Engenharia Oceânica, COPPE, da Universidade Federal do Rio de Janeiro, como parte dos requisitos necessários à obtenção do título de Mestre em Engenharia Oceânica.

Orientadores: Nelson Violante Carvalho
Luiz Mariano Paes de Carvalho
Filho

Rio de Janeiro
Fevereiro de 2022

EVALUATION OF A LINEAR EXPRESSION FOR RETRIEVAL OF
DIRECTIONAL WAVE SPECTRA FROM COMPLEX SAR LOOK CROSS
SPECTRA

Yuri de Oliveira Brasil Corrêa

DISSERTAÇÃO SUBMETIDA AO CORPO DOCENTE DO INSTITUTO
ALBERTO LUIZ COIMBRA DE PÓS-GRADUAÇÃO E PESQUISA DE
ENGENHARIA DA UNIVERSIDADE FEDERAL DO RIO DE JANEIRO COMO
PARTE DOS REQUISITOS NECESSÁRIOS PARA A OBTENÇÃO DO GRAU
DE MESTRE EM CIÊNCIAS EM ENGENHARIA OCEÂNICA.

Orientadores: Nelson Violante Carvalho
Luiz Mariano Paes de Carvalho Filho

Aprovada por: Prof. Nelson Violante Carvalho
Prof. Jesus Portilla Yandun
Prof. Rodrigo Alonso Hauser
Prof. Leandro Farina
Prof. Pedro Veras Guimarães
Prof. José Antonio Moreira Lima

RIO DE JANEIRO, RJ – BRASIL
FEVEREIRO DE 2022

Corrêa, Yuri de Oliveira Brasil

Evaluation of a Linear Expression for Retrieval of Directional Wave Spectra from Complex SAR Look Cross Spectra/Yuri de Oliveira Brasil Corrêa. – Rio de Janeiro: UFRJ/COPPE, 2022.

XIII, 36 p.: il.; 29, 7cm.

Orientadores: Nelson Violante Carvalho

Luiz Mariano Paes de Carvalho Filho

Dissertação (mestrado) – UFRJ/COPPE/Programa de Engenharia Oceânica, 2022.

Referências Bibliográficas: p. 32 – 36.

1. SAR Synthetic Aperture Radar. 2. wave spectra.
3. Linear Inversion. I. Carvalho, Nelson Violante *et al.* II. Universidade Federal do Rio de Janeiro, COPPE, Programa de Engenharia Oceânica. III. Título.

*Dedico este trabalho ao meu pai,
que apesar de não estar mais
presente entre nós, esteve
presente em espírito, em todos os
momentos desafiadores de minha
trajetória acadêmica. Sem sua
dedicação como pai, eu não teria
acesso à educação de qualidade e
gratuita que tive a honra de
usufruir.*

Agradecimentos

Em primeiro lugar gostaria de me desculpar previamente, caso esqueça de alguém que não consegui nomear neste momento. Esta dissertação foi construída ao longo de muito tempo, com muito esforço, com muita dedicação e com contribuições diversas, cada uma à sua maneira.

Agradeço ao professor Nelson Violante, meu orientador no mestrado e na graduação. Aquele que despertou em mim o gosto pela mecânica das ondas e me trouxe para a oceanografia física de vez. Sua exigência me fez dar passos cada vez maiores e com um senso de responsabilidade cada vez maior com a ciência e com a academia.

Ao professor Alexandre Fernandes, meu coorientador de graduação que me deu a incrível oportunidade de ser monitor de oceanografia dinâmica por muito tempo. Com ele aprendi muito sobre a prática docente, o que inclui a preparação de listas, provas e aulas. Aprendi como um professor pode ser exigente e cuidadoso ao mesmo tempo, humano e respeitoso com seus alunos.

Ao professor Luiz Mariano, meu coorientador neste trabalho, Professor entusiasmado, perspicaz e extremamente competente. Seu modo de discutir ciência, direto, exigente e profissional foi imprescindível para que eu pudesse dar o melhor de mim para este trabalho.

À toda equipe do Laboratório de Instrumentação Oceanográfica (LIOc), em especial à Júlia, Pedro, Guilherme, Izabel, Ítalo, Lilian, Jorge, Fábio, Henrique e é claro, ao Professor Carlos Parente, exemplo de ser humano e docente.

À equipe do Laboratório de Métodos Computacionais em Engenharia (LAMCE), que esteve convivendo comigo durante boa parte dessa caminhada e sempre me apoiou, além de trazer alegria em momentos de muito trabalho e estresse.

Ao restante da equipe envolvida com o SARmulator. Ao Felipe que trabalhou muito próximo a mim e me ajudou inúmeras vezes com a humildade e a calma de sempre, e que tem uma parcela enorme na confecção deste trabalho. Ao André, que por inúmeras vezes discutiu equações comigo por telefone e clareou minha mente quando tudo parecia muito confuso e difícil. Ao Carlos com quem tenho trabalhado na confecção de um SARmulator escrito em python. Ao Leonardo que entrou há pouco tempo no grupo mas que já nos traz a certeza de que trabalhos de alta qualidade irão surgir.

À Faculdade de Oceanografia (FAOC) e seu corpo docente, que moldou o profissional que sou hoje. Em especial à professora Gleicy e ao professor Alessando. Estes sempre amigos e solícitos para quaisquer assuntos e necessidades.

À minha mãe e irmã que sempre acreditaram em mim e no meu sonho de trabalhar para a academia e fazer ciência de qualidade internacional. Apoios imprescindíveis para essa jornada.

Aos meus amigos, que sempre torceram por mim e acreditaram em cada passo que dei desde a graduação até o mestrado. Aqueles que são minha segunda família, que eu faria qualquer coisa por eles. E àqueles que já se foram, mas que carrego comigo para onde quer que eu vá.

Agradeço principalmente, à Paola Groberio, uma pessoa especial que esteve ao meu lado me dando um apoio inacreditável por boa parte do mestrado. Agradeço a todas as palavras de força e motivação que ouvi em meio ao estresse, ansiedade e dúvidas sobre a minha capacidade. Obrigado por tudo.

Resumo da Dissertação apresentada à COPPE/UFRJ como parte dos requisitos necessários para a obtenção do grau de Mestre em Ciências (M.Sc.)

AVALIAÇÃO DE UMA EXPRESSÃO LINEAR PARA RECUPERAÇÃO DE
ESPECTROS DIRECIONAIS DE ONDA A PARTIR DE ESPECTROS
CRUZADOS DE IMAGENS COMPLEXAS

Yuri de Oliveira Brasil Corrêa

Fevereiro/2022

Orientadores: Nelson Violante Carvalho

Luiz Mariano Paes de Carvalho Filho

Programa: Engenharia Oceânica

A viabilidade de um método de inversão linear, aplicado a espectros cruzados complexos de imagens SAR para recuperar espectros direcionais de ondas, é investigada. O método proposto é computacionalmente eficiente e não requer nenhuma informação *a priori* de modelos de ondas ou atmosféricos. Vários casos teste de espectros de imagens SAR complexos foram simulados considerando uma ampla gama de valores de esbeltez de onda para diferentes configurações de satélites. Os resultados dos casos simulados foram empregados para corrigir viés, ao passo que espectros direcionais obtidos de espectros cruzados de Nível 1 são recuperados. As não linearidades, não contabilizadas na aplicação da inversão linear, são quantificáveis, pois dependem da configuração do satélite e da posição relativa do espectro de onda de pico em relação ao *cut-off* azimutal. Os espectros de onda recuperados com o Método de Inversão Linear de um *ground track* do Envisat foram avaliados contra a reanálise ECMWF, ERA5, e comparados com os resultados dos espectros do modo onda ESA Nível 2 WWV. Ambos métodos apresentaram resultados semelhantes em termos de RMSE e SI para altura significativa, comprimento de onda de pico e direção de propagação de pico. A forma dos espectros direcionais de onda recuperados com o Método de Inversão Linear apresentou melhor similaridade com os espectros ERA5, em comparação com os espectros WWV. Além disso, em cerca de um terço dos casos, o método ESA não resolveu a ambiguidade direcional. Os resultados preliminares empregando o Método de Inversão Linear são promissores, especialmente considerando sua simplicidade e desempenho contra os espectros de ondas obtidos pela ESA.

Abstract of Dissertation presented to COPPE/UFRJ as a partial fulfillment of the requirements for the degree of Master of Science (M.Sc.)

EVALUATION OF A LINEAR EXPRESSION FOR RETRIEVAL OF
DIRECTIONAL WAVE SPECTRA FROM COMPLEX SAR LOOK CROSS
SPECTRA

Yuri de Oliveira Brasil Corrêa

February/2022

Advisors: Nelson Violante Carvalho

Luiz Mariano Paes de Carvalho Filho

Department: Ocean Engineering

The feasibility of a Linear Inversion Method applied to SAR cross spectra to retrieve wave directional spectra is investigated. The proposed method is computationally efficient and does not require any *a priori* information from wave or atmospheric models. Several test cases of complex SAR image spectra were simulated considering a broad range of values of steepness for different satellite configurations. The results of the simulated cases were employed to correct biases while retrieving directional wave spectra from Level 1 cross spectra. The nonlinearities, not accounted for when applying a linear inversion, are quantifiable as they depend on the satellite configuration and the relative position of the peak wave spectrum in relation to the azimuth cut-off. The wave spectra retrieved with the Linear Inversion Method from an Envisat ground track were evaluated against the ECMWF reanalysis ERA5 and compared to the results of ESA Level 2 WWV wave mode spectra. Both methods presented similar results in terms of RMSE and SI for significant wave height, peak wavelength and peak propagation direction. The shape of the directional wave spectra retrieved with the Linear Inversion Method presented better similarity with the ERA5 spectra, in comparison with the WWV spectra. Moreover, in around one third of the cases, the ESA method did not resolve the directional ambiguity. The preliminary results employing the Linear Inversion Method are encouraging, specially considering its simplicity and performance against the ESA distributed wave spectra.

Sumário

Lista de Figuras	x
Lista de Tabelas	xiii
1 Introduction	1
2 Mathematical Model	5
2.1 Simulated Complex SAR Image Cross Spectra	6
2.2 The Linear Inversion Method (LIM)	8
2.3 Simulations and Inverted SAR Wave Spectra	9
3 Nonlinearities in the Mapping Mechanism	13
4 Simulated Test Cases	16
5 Envisat ASAR Level 1 Cross Spectra (WVS)	23
6 Summary and Conclusions	29
Referências Bibliográficas	32

Lista de Figuras

2.1	Schematic description of the simulator of complex SAR look cross spectra — adapted from [23].	6
2.2	Ocean wave imaging mechanism using the simulator of SAR cross spectra. The simulated wave spectrum (a), a swell with $H_s=2.5$ m, $L_p=585$ m, $\sigma = 20^\circ$ and azimuthal peak propagation direction ($\phi_p = 0^\circ$). The nonlinear forward mapping (Equation 2.9) is applied to (a) to obtain the real part (c) and imaginary part (d) of the SAR cross spectrum, whilst (b) is the real part computed with the linear forward mapping (Equation 2.12). Azimuth cut-off $L_{cut}=88$ m.	10
2.3	Similar to Figure 2.2 for a simulated bimodal wave spectrum, with a swell propagating in the positive azimuth direction ($H_s=2.5$ m, $L_p=585$ m, $\sigma = 20^\circ$ and $\phi_p = 0^\circ$) and a windsea component propagating in the range direction ($H_s=3.0$ m, $L_p=205$ m, $\sigma = 33^\circ$ and $\phi_p = 90^\circ$). Azimuth cut-off $L_{cut}=219$ m.	11
2.4	Retrieved wave spectra employing the LIM; (a) corresponding to the simulation depicted in Figure 2.2(a) and (b) corresponding to the simulation depicted in Figure 2.3(a). The peak wavelengths and directions are fairly well represented, apart from a reduction in \hat{H}_s	12
3.1	Ocean wave imaging mechanism using the simulator of complex image cross spectra. A simulated bimodal wave spectrum (a), with a swell propagating in the positive range direction ($H_s=2.0$ m, $L_p=455$ m and $\sigma = 20^\circ$) and a windsea component propagating in the azimuthal direction ($H_s=3.0$ m, $L_p=205$ m and $\sigma = 24^\circ$). The real part of its linear SAR cross spectrum is shown in (b), whilst (c) is the real part of the nonlinear image spectrum. In (d), the retrieved wave spectrum using the LIM. Azimuth cut-off $L_{cut}=211$ m.	14

- 4.1 From left to right: relationship between L_p and L_{cut} for azimuth, intermediate and range travelling waves, assuming the Envisat configuration. The dashed line shows when L_p equals L_{cut} and can be think of a delimiter between nonlinear (above the line) and linear (below the line) SAR mapping of the wave component. The colors represent distinct values of H_s . For each combination of H_s and L_p a SAR cross spectrum was simulated employing the integral forward mapping relation. The three panels show the combinations in which the retrieved spectra passed the consistency test. 17
- 4.2 Relative error of \hat{H}_s for azimuthal (0° – blue square), intermediate (45° – green triangle) and range (90° – orange circle) directions — for Envisat (a) and for Sentinel-1 (b) configurations. The vertical axis is \mathcal{E}^{H_s} , the relative error between simulated and retrieved significant wave height. The negative sign in \mathcal{E}^{H_s} indicates underestimation. The horizontal axis is P_{cut} , the relative distance between \hat{L}_p and L_{cut} . The vertical dashed line shows when $\hat{L}_p = L_{cut}$. Negative values of P_{cut} indicate that \hat{L}_p is smaller than L_{cut} and nonlinear effects become relevant. Also shown the number of entries N and the best fit of the data. 18
- 4.3 Scatter plots of retrieved versus simulated significant wave height, for Envisat (left column) and Sentinel-1 (right column) before (first row) and after (second row) the empirical corrections shown in Figure 4.2. For the three reference directions. Also shown the statistical parameters for each direction (on the left) and the whole data set (on the right). 19
- 4.4 Top line: relative error of \hat{L}_p for azimuthal (0° – blue square), intermediate (45° – green triangle) and range (90° – orange circle) directions — for Envisat (a) and for Sentinel-1 (b) configurations. The horizontal axis is P_{cut} , the relative distance between \hat{L}_p and L_{cut} . The vertical dashed line shows when $\hat{L}_p = L_{cut}$. The vertical axis is \mathcal{E}^{L_p} and the positive sign indicates superestimation. Bottom line: values of \hat{L}_p after the empirical corrections depicted in the top line. Also shown the number of entries N and the best fit of the data. 21

4.5	<p>Top line: absolute error of $\hat{\phi}_p$ for azimuthal (0° – blue square), intermediate (45° – green triangle) and range (90° – orange circle) directions — for Envisat (a) and for Sentinel-1 (b) configurations. The horizontal axis is P_{cut}. The vertical dashed line shows when $\hat{L}_p = L_{cut}$. The vertical axis is \mathcal{E}^{ϕ_p}, the absolute difference between retrieved and simulated ϕ_p. Positive values of \mathcal{E}^{ϕ_p} indicate that the waves are rotating into the range direction with respect to the simulated direction. Only waves propagating in the intermediate direction are affected. Bottom line: values of $\hat{\phi}_p$ after the empirical corrections depicted in the top line. Also shown the number of entries N and the best fit of the data.</p>	22
5.1	<p>Segment of Envisat ground track 0383 on 18 January 2009 around 15:09 UTC, with 109 spectra. The figures describe their spatial distribution. . . .</p>	24
5.2	<p>Scatterplots of, respectively, H_{s10} (a and b), ϕ_{p10} (c and d) and L_{p10} (e and f). For the ERA5 against the LIM (left column) and ERA5 against WWW (right column). Also shown the Pearson correlation (r), Mean, Standard Deviation (Std), Bias, Root Mean Square Error (RMSE), Scatter Index (SI) and number of entries (N) — 87 cases passed the homogeneity tests. . . .</p>	25
5.3	<p>The parameter Ω (Equation 5.1) is a matrix square error normalized with the square of the reference wave spectrum (ERA5), computed along the ground track shown in Figure 5.1. Small values of Ω indicate close proximity between spectra. For wave spectra retrieved with the LIM (green diamond) and with the ESA procedure (WWW, pink circle). Also shown, as red circles, the cases where the directional ambiguity was not properly resolved (WWW - Amb) — Equation 5.2.</p>	27

Lista de Tabelas

2.1	Wave and satellite parameters employed as input for the SAR complex image simulations.	5
-----	--	---

Capítulo 1

Introduction

The Synthetic Aperture Radar (SAR) can yield the directional wave spectrum, with the known limitations in the azimuthal high frequency band defined by a wavelength threshold — the so called azimuth cut-off [16]. A myriad of satellites — such as ERS-1&2, RADARSAT, Envisat and the currently operational Sentinel1-A&B twins — encompass nearly 30 years of continuous data with tens of millions of observations globally distributed. In their seminal paper, HASSELMANN e HASSELMANN [7] proposed an analytic relationship for the mapping of a wave spectrum into a SAR image spectrum, the forward mapping relation, employing Modulation Transfer Functions — MTF's, the more relevant are named Hydrodynamic, Tilt and Velocity Bunching [6]. The nonlinear forward mapping relation for the SAR image variance spectrum was a major achievement, with their expression later extended to include the SAR look cross spectrum [5].

The satellite operation modes are programmed to yield either a single intensity image or a sequence of images [21]. Some of the schemes to retrieve wave directional spectra from SAR are based on single images, therefore additional information, in general from wave models, are employed to solve the inherent 180° directional ambiguity — and in some instances to fill in as well the lack of spectral information in the high wavenumber band [8, 24]. In coastal waters, the satellites are in most occasions switched to a single intensity image mode and the use of an input first guess is desirable [32]. Using complex images, two overlapping looks separated by a fraction of a second are employed, computing their cross spectra to use phase differences to determine the wave propagation direction [5]. Hence, there is no need for *a priori* information to solve the directional ambiguity, but the lack of high wavenumber information remains.

The mapping of the sea surface by a SAR instrument is a nonlinear and complex process, prone to inaccuracies [19]. The nonlinear distortion induced by motion effects implies that the shorter waves are misplaced on the SAR image plane, imposing a high wavenumber azimuth cut-off beyond which the signal is corrupted and hence not directly mapped [6]. Moreover, the nonlinearities are also associated with shifts of the spectral peak and hence bias in the spectral parameter estimates. These inaccuracies are mainly due to the Velocity Bunching mechanism associated with a moving sea surface caused by the orbital motions of the waves, see discussion for example in ROBINSON [21], VIOLANTE-CARVALHO *et al.* [30], VIOLANTE-CARVALHO e ROBINSON [31]. Therefore the high azimuthal wavenumber region beyond the cut-off, mostly related to the windsea, is associated with the corrupted, nonlinear contribution in the SAR image variance spectrum or the SAR look cross spectrum. However, the lower wavenumber spectral band is a quasi-linear contribution from the longer, swell waves, containing retrievable information. The exact, nonlinear, forward relation is computationally demanding and its linear or quasi-linear forms are — in many instances — an acceptable approximation for the mapping of the SAR cross spectrum [3, 18]. LEHNER *et al.* [12] employed a quasi-linear forward mapping relation to compare around one thousand of ERS-2 SAR Wave Mode spectra against collocated deep water spectra estimated with the European Centre for Medium-Range Weather Forecasts (ECMWF). Their analysis was mainly restricted to wave propagation directions derived from the imagettes, with a good agreement reported. No qualitative analysis was presented, in particular about the azimuth cut-off wavelength, in respect to the peak wavelength and direction of the imaged waves.

More importantly in terms of retrieval applications, HASSELMANN e HASSELMANN [7] also proposed a solution to extract the wave spectrum from a SAR cross spectrum. Because of the directional ambiguity and loss of information beyond the azimuth cut-off, a rigorous inverse mapping solution does not exist. The retrieval algorithms apply methods to minimise the differences between the measured SAR spectrum and its counterpart computed using the forward mapping, in general employing a first guess wave spectrum or wind information to estimate the windsea spectrum. Several schemes have been proposed for retrieving wave spectra from SAR data, with distinct approaches [cf., among others, 1, 3–5, 7, 8, 11, 18, 24].

In HASSELMANN e HASSELMANN [7], KROGSTAD *et al.* [11] and HASSELMANN *et al.* [8], based on a first-guess wave spectrum to solve the ambiguity and to fill in the high wavenumber band, an iterative scheme was used for inverting the integral nonlinear forward mapping relation. A similar approach was employed in SCHULZ-STELLENFLETH e LEHNER [24], but using the cross spectrum to remove the directional ambiguity. In these approaches, the high wavenumber part of

the retrieved spectrum was retained from the first-guess wave spectrum.

MASTENBROEK e DE VALK [18], on the other hand, employed a simplified retrieval method, without the use of any *a priori* wave information. Using Hasselmann’s nonlinear forward mapping and wind measurements from a scatterometer operating simultaneously with the SAR, the windsea spectrum was computed. This nonlinear contribution in the high wavenumber band was subsequently subtracted from the measured SAR cross spectrum and the resulting spectrum was inverted, retrieving the swell spectrum. Their retrieval scheme was validated against several directional buoys with no evident bias reported for components longer than 225 m. The propagation direction was quite accurate, with errors of the same order of the directional resolution of the ERS-1&2 SAR Wave Mode data.

In a similar approach, CHAPRON *et al.* [3] used the residual SAR cross spectrum after subtraction from the windsea to compute the swell spectrum. However, the nonlinear contribution beyond the azimuth cut-off was not retained, with the retrieved wave spectrum hence restricted to the low wavenumber part directly measured with the SAR. The retrieved wave spectrum being, therefore, a representation of the longer waves only. This is the retrieval method currently employed by the European Space Agency (ESA) to generate the Level 2 WWV product — the SAR wave mode spectra. It does not require any *a priori* wave information, but the wind speed and direction — in general from numerical models — are necessary as input to iteratively estimate the windsea component.

The Advanced SAR (ASAR) Wave Mode distributed by ESA consists of three products. The WVI product comprises the single-look complex (SLC) imagettes, generated from Level 0. The SAR cross-spectra — the Level 1B WVS product — are extracted from the SLC imagettes and are used as input for the SAR inversion schemes. And the Level 2 WWV product, the inverted wave spectra, are provided on a log-polar grid. Validations of the WWV spectra, in particular significant wave height, have been performed against *in situ*, altimeter and model data [see, for instance, 9, 14, 34]. Systematic evaluations of the WWV spectral shape have not been presented so far, although discrepancies with model estimates have been reported [13, 19].

Distortions in the azimuth high frequency band impose limitations in the retrieval of significant wave height, the most commonly used wave parameter, requiring external information to fill in the spectral gap — a challenging problem and prone to model inaccuracies [8, 18]. Additionally, to avoid the complex task to retrieve the wave spectrum using inversion schemes, [26] proposed a technique to empirically estimate parameters directly from the ERS SAR images — which hence does not require the use of *a priori* information. Their approach was adapted to other satellite missions such as RADARSAT [22], Envisat [15] and Sentinel-1 [20, 28], using

roughly the same procedure to estimate wave parameters from SAR image parameters. With a different approach, [33] proposed a semiempirical expression relating significant wave height to peak wavelength, peak propagation direction and cut-off wavelength. Differently from the empirical relations for significant wave height that rely on large data sets to fit the SAR image parameters and have to be tuned accordingly, the expression in [33] can be applied to any SAR mission and also does not require any external information.

Simulators are important tools for analysing and evaluating different wave spectra retrieval methods, among other applications. SANTOS *et al.* [23] presented an algorithm to simulate SAR image spectra of ocean swell waves. The simulator is based on Hasselmann's forward mapping relation with sound MTF's that account for the main physical processes involved in the imaging of ocean waves. Simulators can also be employed to evaluate the impact of *a priori* information on the retrieval process, pinpointing possible shortcomings.

Our objective is to investigate the effectiveness of a Linear Inversion Method (referred to in the following as LIM) as a tool to retrieve wave spectra. Using the SAR cross spectra as only input — no wave or wind *a priori* information is required — the retrieved wave spectrum is therefore restricted to the low wavenumber band. The analytically simple and computationally low cost method is evaluated and its accuracy to retrieve the directional wave spectrum is assessed. For this purpose, the single intensity image spectrum simulator described in [23] is employed, here extended to compute the complex SAR image cross spectrum. With prescribed, known input wave spectra, the nonlinear forward mapping relation is adapted to generate the simulated SAR cross spectra. Parameters of the input wave spectra — such as significant wave height, peak wavelength and peak propagation direction — are perturbed and the retrieved wave spectra using the LIM are evaluated against the input, ground truth, simulated wave spectra. Additionally, WVS Cross Spectra from an Envisat ground track over the swell infested Pacific Ocean are also used as input to the LIM and the retrieved wave spectra are evaluated against collocated deep water ECMWF reanalysis ERA5 spectra and against WWV spectra.

The remaining is structured as follows: in chapter 2, a description of the theoretical approach and terminology is presented, whereas nonlinearities of the SAR imaging mechanisms are illustrated with simulations in chapter 3. In chapter 4, the results using the cross spectra image simulator are discussed. The retrieved wave spectra with the LIM using Envisat WVS cross spectra as input are evaluated against ERA5 and WWV spectra in chapter 5. Finally, chapter 6 summarises our main conclusions.

Capítulo 2

Mathematical Model

The simulations are based on the implementation of two essential computational processes. The first is to simulate parametric forms of an SAR cross spectrum as function of the quantities that describe the oceanic condition and the parameters that define the configuration of the satellite used in the observation. Secondly, the ocean wave spectrum retrieved from the inversion of the simulated SAR cross spectrum is evaluated.

Let $\mathbf{o} = (H_s, \phi_p, L_p, \sigma)$ be the sea state vector and $\mathbf{s}_\tau = (h, \Phi, p, U, \alpha, \nu, \tau)$ the remote sensing vector; its components are listed in Table 2.1. Hence, the simulations can be briefly described by

$$\Psi^{ret} = \mathbf{I}_{\mathbf{s}_\tau} \circ \mathbf{C}_{\mathbf{o}}^{\mathbf{s}_\tau}, \quad (2.1)$$

namely, the retrieved wave spectrum Ψ^{ret} is the composition between the inversion mechanism $\mathbf{I}_{\mathbf{s}_\tau}$ and the complex SAR image spectrum $\mathbf{C}_{\mathbf{o}}^{\mathbf{s}_\tau}$ — with \circ as the function composition symbol.

Tabela 2.1: Wave and satellite parameters employed as input for the SAR complex image simulations.

symbol	parameter	symbol	parameter
	Sea State		Sensor
H_s	significant wave height	h	satellite altitude
ϕ_p	peak wave direction (w.r.t. satellite flight)	Φ	orbit inclination
L_p	peak wavelength	p	radar polarisation
σ	directional spreading	U	satellite velocity
	Geophysical	α	radar incidence angle
v	wind speed	ν	radar look direction
		τ	time lag

2.1 Simulated Complex SAR Image Cross Spectra

The time evolution of the ocean wave field within the span of two images is employed to compute the complex SAR image cross spectrum. The disambiguation of the wave propagation direction is achievable, contained in its phase [1, 5, 35] — with its magnitude related to the wave energy. In the following, the adaptations to the method developed by [23] to simulate parametric forms of SAR cross spectra are presented.

Wave and satellite parameters are employed as input for the SAR image simulations, comprising respectively the \mathbf{o} -stage (ocean) and \mathbf{s}_τ -stage (satellite), as depicted in Figure 2.1. In the \mathbf{o} -stage, sea state parameters yield a simulated directional spectrum employing a JONSWAP frequency spectrum model and a power-cosine (\cos^{2s}) directional spreading model [17]. During the \mathbf{s}_τ -stage, the mapping ocean - image cross spectrum is adjusted to the remote sensing parameters.

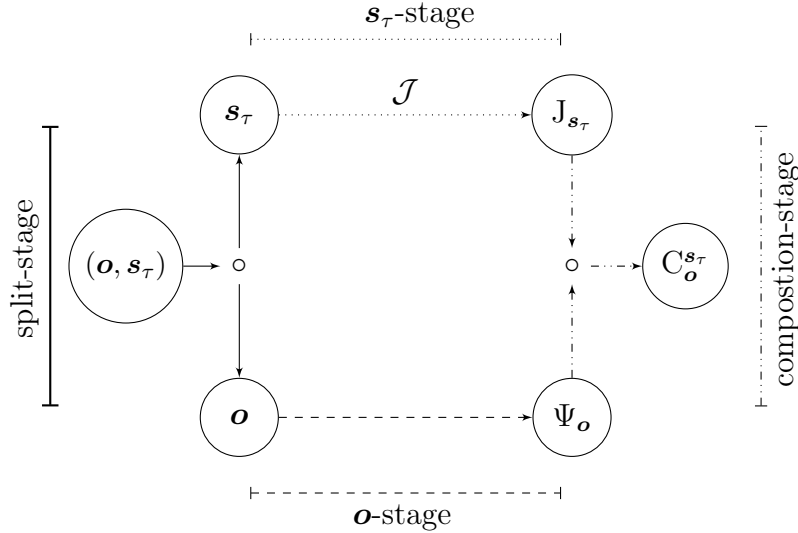


Figure 2.1: Schematic description of the simulator of complex SAR look cross spectra — adapted from [23].

However, for SAR cross spectra, there is a time lag between images, a fraction of a second apart represented by τ and described in the \mathbf{s}_τ -stage. When τ equals zero, the procedure is reduced to the single intensity image approach. Otherwise, as is the case here implemented, the SAR cross spectrum is computed. The \mathbf{s}_τ -stage is defined by the mapping $\mathbf{s}_\tau \mapsto \mathbf{J}_{\mathbf{s}_\tau}$ between the satellite configuration and the complex forward mapping [5]. The forward mapping $\mathbf{J}_{\mathbf{s}_\tau}$ relates the wave spectrum $\Psi_{\mathbf{o}}$ — for a sea state vector \mathbf{o} — to the respective complex SAR image spectrum $\mathbf{C}_{\mathbf{o}}^{\mathbf{s}_\tau}$, in the form

$$\mathbf{J}_{\mathbf{s}_\tau} \circ \Psi_{\mathbf{o}} = \mathbf{C}_{\mathbf{o}}^{\mathbf{s}_\tau} \quad (2.2)$$

where

$$\mathbf{C}_o^{s\tau} = \mathbf{Q}_o^{s\tau} + \text{higher-order nonlinearities.} \quad (2.3)$$

$\mathbf{Q}_o^{s\tau}$ is the quasi-linear approximation of the cross spectrum $\mathbf{C}_o^{s\tau}$, given — when evaluated at the wave component \mathbf{k} — by

$$\mathbf{Q}_o^{s\tau}(\mathbf{k}) = 0.5 e^{-k_x^2 \beta^2 \rho^u(0)} \left[e^{i\omega\tau} |T_{(sar)}^s(\mathbf{k})|^2 \Psi_o(\mathbf{k}) + e^{-i\omega\tau} |T_{(sar)}^s(-\mathbf{k})|^2 \Psi_o(-\mathbf{k}) \right]. \quad (2.4)$$

Here, k_x and k_y denote azimuth and range components of \mathbf{k} respectively. Also, $\beta = d/U$ is the ratio between the slant range d and the SAR platform velocity U . The orbital velocity variance is the term $\rho^u(\mathbf{0})$ and ω is the radian frequency. The exponential term ($\exp[-k_x^2(\beta)^2 \rho^u(\mathbf{0})]$) is a cut-off factor, which is a — sea state dependent — azimuthal low pass filter in the spectral domain. Moreover, the theoretical value of the azimuth cut-off wavelength is given by [10, 16]

$$L_{cut} = \pi \sqrt{\beta^2 \rho^u(\mathbf{0})}. \quad (2.5)$$

The main modulation effects — namely, Tilt, Hydrodynamic, Range Bunching and Velocity Bunching — are present in the image cross spectrum through the SAR transfer function, expressed by

$$T_{(sar)}^{s\tau}(\mathbf{k}) = T_{(rar)}^{s\tau}(\mathbf{k}) + T_{(vb)}^{s\tau}(\mathbf{k}), \quad (2.6)$$

where

$$T_{(rar)}^{s\tau}(\mathbf{k}) = \frac{-4\iota k_y \cot \alpha}{1 + \sin^2 \alpha} + 4.5 \omega \frac{k_y^2 \omega - \iota \vartheta}{|k| \omega^2 + \vartheta^2} - \iota k_y \cot \alpha \quad (2.7)$$

is the RAR (Real Aperture Radar) MTF with vertical polarisation in transmit and receive (VV) and right looking radar, α is the radar incidence angle and ϑ is the hydrodynamic relaxation rate equal to 0.5 s^{-1} [see details in 7]. In Equation (2.7), the Tilt MTF is the first term on the right-hand side, the Hydrodynamic MTF is the second term and the Range Bunching MTF is the last term. Additionally, the Velocity Bunching MTF is

$$T_{(vb)}^{s\tau}(\mathbf{k}) = -\iota \beta k_x \omega \left(\frac{k_y}{k} \sin \alpha + \iota \cos \alpha \right). \quad (2.8)$$

The truncated version of Equation (2.3) can be used to compute the nonlinear forward mapping numerically [7] as

$$\mathbf{C}_o^{s\tau}(\mathbf{k}) = e^{-k_x^2 \beta^2 \rho^u(0)} \sum_{n=1}^6 \sum_{m=2n-2}^{2n} (k_x \beta)^m R_{n,m}[\mathbf{o}, \mathbf{s}_\tau](\mathbf{k}). \quad (2.9)$$

The sixth order truncation of the infinite series is a good approximation of the complex SAR image spectrum, retaining most of its features [7, 8]. Moreover, the term $R_{n,m}[\mathbf{o}, \mathbf{s}_\tau]$ represents the spectral factor related to $\Psi_{\mathbf{o}}$, which regulates the effects of modulations caused by the ocean waves and transferred to the image. Index n is the nonlinearity order with respect to the input wave spectrum whilst m is the order with respect to the velocity bunching parameter. Denoting $\mathbf{s} = (h, \Phi, p, U, \alpha, \nu)$, when $\tau = 0$

$$\mathbf{C}_{\mathbf{o}}^{s_0}(\mathbf{k}) = \mathbf{P}_{\mathbf{o}}^s(\mathbf{k}), \quad (2.10)$$

where $\mathbf{P}_{\mathbf{o}}^s(\mathbf{k})$ is the auto-spectrum of the SAR image, which demonstrates that the presented method is an extension of [23]. Thus, the complex simulator is designed to receive as input the wave and satellite parameters and generate as output the corresponding directional wave spectrum and the linear and nonlinear forms of the SAR image cross spectrum.

2.2 The Linear Inversion Method (LIM)

Equation (2.2) is the forward mapping relation of a directional wave spectrum onto its SAR cross spectrum. However, the ocean wave spectrum is not known *a priori*, therefore characterising an inverse problem. The technique here employed consists of finding the optimal ocean wave spectrum Ψ^{ret} whose corresponding linear approximation of the image cross spectrum has the minimum distance to the simulated cross spectrum $\mathbf{C}_{\mathbf{o}}^{s_\tau}$. In other words,

$$\Psi^{ret}(\mathbf{k}) = \arg \min_{\zeta(\mathbf{k}) \geq 0} \int |(\mathbf{L}_{\zeta}^{s_\tau}(\mathbf{k}) - \mathbf{C}_{\mathbf{o}}^{s_\tau}(\mathbf{k}))|^2 d\mathbf{k}, \quad (2.11)$$

where

$$\mathbf{L}_{\zeta}^{s_\tau}(\mathbf{k}) = 0.5 \left[e^{i\omega\tau} \left| T_{(sar)}^{s_\tau}(\mathbf{k}) \right|^2 \zeta(\mathbf{k}) + e^{-i\omega\tau} \left| T_{(sar)}^{s_\tau}(-\mathbf{k}) \right|^2 \zeta(-\mathbf{k}) \right] \quad (2.12)$$

is the linear approximation of the SAR cross spectrum related to the ocean wave spectrum $\zeta(\mathbf{k})$. Equation (2.12) allows to obtain analytically the function that performs the minimum value of the nonlinear functional (2.11). According to [27],

$$\psi^{ret}(\mathbf{k}) = \begin{cases} \varphi(\mathbf{k}), & \text{if } \varphi(\mathbf{k}) \geq 0 \wedge \varphi(-\mathbf{k}) \geq 0 \\ 2 |T_{(sar)}^{s\tau}(\mathbf{k})|^{-2} \Re \{ \exp(-i\omega t) \mathbf{C}_o^{s\tau}(\mathbf{k}) \}, & \text{if } \Re \{ \mathbf{C}_o^{s\tau}(\mathbf{k}) \overline{T_{(sar)}^{s\tau}(\mathbf{k})} \} \geq 0 \wedge \varphi(-\mathbf{k}) < 0 \\ 0, & \text{if } \Re \{ \mathbf{C}_o^{s\tau}(\mathbf{k}) \overline{T_{(sar)}^{s\tau}(\mathbf{k})} \} < 0 \wedge \Re \{ \mathbf{C}_o^{s\tau}(\mathbf{k}) (T^s(-\mathbf{k})) \} < 0 \end{cases} \quad (2.13)$$

where

$$\varphi(\mathbf{k}) = \frac{\sin(\omega\tau) \Re \{ \mathbf{C}_o^{s\tau}(\mathbf{k}) \} + \cos(\omega\tau) \Im \{ \mathbf{C}_o^{s\tau}(\mathbf{k}) \}}{|T_{(sar)}^{s\tau}(\mathbf{k})|^2 \sin(\omega\tau) \cos(\omega\tau)} \quad (2.14)$$

and the overbar means average value. In this way, the linear inversion mechanism $\mathbf{I}_{s\tau}$ is finally defined by

$$\mathbf{I}_{s\tau} \circ \mathbf{C}_o^{s\tau} = \Psi^{ret}. \quad (2.15)$$

Clearly, the function $\mathbf{I}_{s\tau}$ is not linear but is referred as such with a slight abuse of terminology because of Equation (2.12).

This inversion mechanism has a clear advantage over single look methods, since the 180° directional ambiguity is corrected without the need of additional information. The experiments discussed in the following consist of simulations of image cross spectra and their subsequent linear inversion with comparative analysis of the wave parameters used as input to the system. In this sense, the parameters computed from the retrieved directional wave spectra will define the retrieved vector $\hat{\mathbf{o}} = (\hat{H}_s, \hat{\phi}_p, \hat{L}_p, \hat{\sigma})$ — \hat{H}_s is therefore the retrieved significant wave height and so on.

2.3 Simulations and Inverted SAR Wave Spectra

Figure 2.2 shows an example of the forward mapping relations. The simulations are performed using Sentinel-1 parameters [of altitude, orbit inclination and look direction, to name a few, listed, for example, in 23, and in <http://www.esa.int>]. The upper left panel is the simulated directional wave spectrum with $L_p=585$ m, $H_s=2.5$ m and propagating in the positive azimuth direction ($\phi_p = 0^\circ$). The computed azimuth cut-off wavelength L_{cut} is equal to 88 m, hence way below L_p . The upper right panel shows the SAR image spectrum (real part) using the linear forward mapping (Equation 2.12), whereas the lower panels are the real part (c) and imaginary part (d) computed with the full, nonlinear forward mapping relation (Equation 2.9). The positive peak in the imaginary part of the image spectrum indicates the correct propagation direction [1, 5], therefore enabling the determination of the unambi-

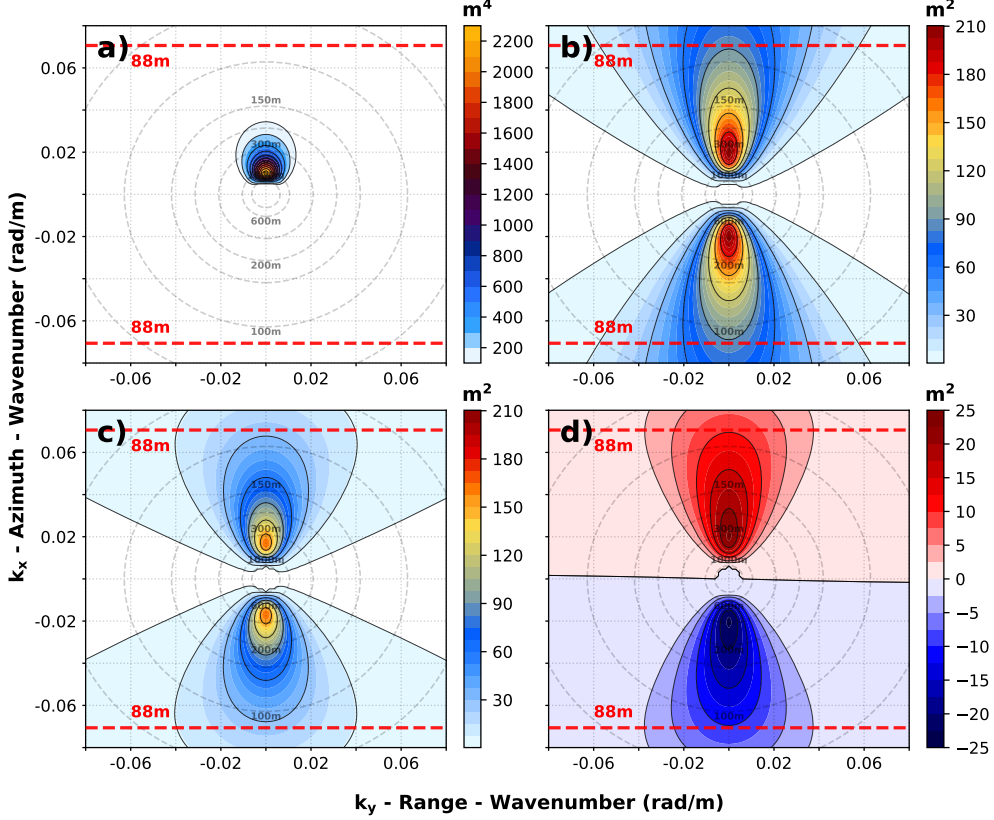


Figure 2.2: Ocean wave imaging mechanism using the simulator of SAR cross spectra. The simulated wave spectrum (a), a swell with $H_s=2.5$ m, $L_p=585$ m, $\sigma = 20^\circ$ and azimuthal peak propagation direction ($\phi_p = 0^\circ$). The nonlinear forward mapping (Equation 2.9) is applied to (a) to obtain the real part (c) and imaginary part (d) of the SAR cross spectrum, whilst (b) is the real part computed with the linear forward mapping (Equation 2.12). Azimuth cut-off $L_{cut}=88$ m.

guous direction. The effect of the azimuth cut-off becomes discernible comparing the real parts of the SAR image spectrum (b and c) — since the linear forward mapping does not retain the nonlinear cut-off term which reduces drastically the energy in the high wavenumber band. Nonetheless, both depict clearly the swell peak position, for a linear case where most of the wave energy is above the azimuth cut-off wavelength.

The orbital velocity distribution of the scatterers introduce Doppler shifts during the SAR imaging process, causing azimuthal displacements [6]. When the displacement is small compared to the wavelength of the imaged waves, as is the case in general for swell dominated events, the sea state dependent Velocity Bunching effect (Equation 2.8) is linear, as shown in Figure 2.2 with L_{cut} much smaller than L_p . The nonlinear (2.2c) and linear (2.2b) image spectra are very similar. In such situations, the LIM is a very effective tool imposing minor deformations in the retrieved wave spectrum. However, in windsea dominated events, when the orbital velocities are more randomly distributed, the displacements increase, causing dis-

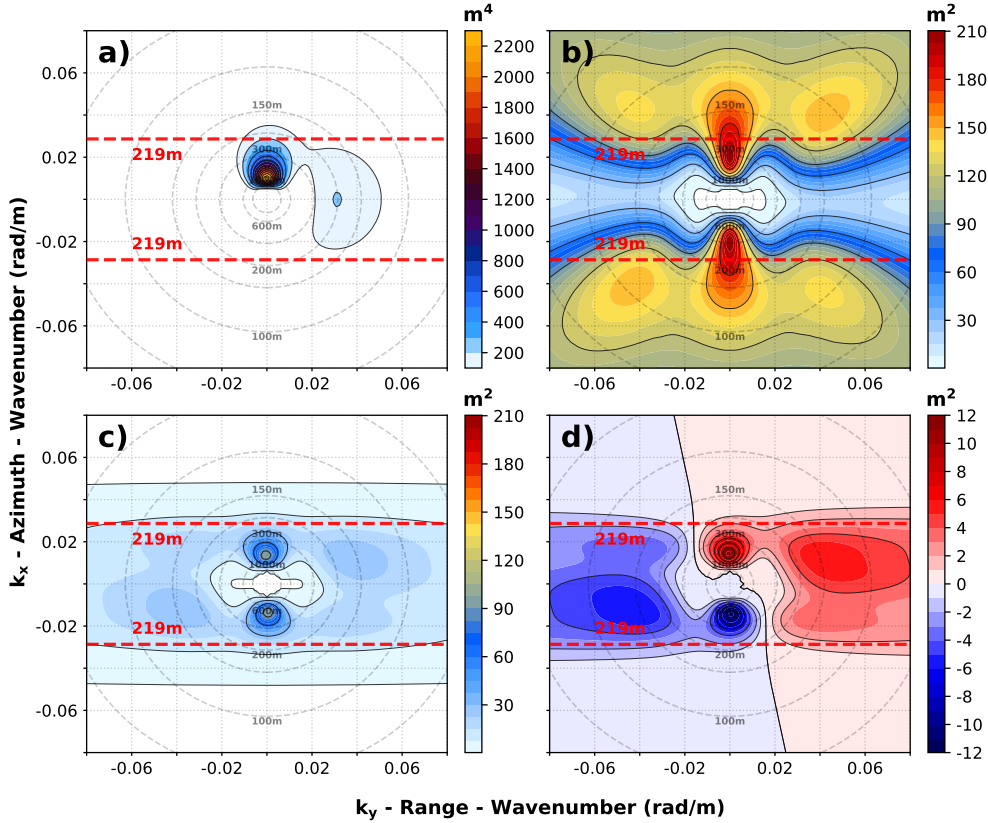


Figure 2.3: Similar to Figure 2.2 for a simulated bimodal wave spectrum, with a swell propagating in the positive azimuth direction ($H_s=2.5$ m, $L_p=585$ m, $\sigma = 20^\circ$ and $\phi_p = 0^\circ$) and a windsea component propagating in the range direction ($H_s=3.0$ m, $L_p=205$ m, $\sigma = 33^\circ$ and $\phi_p = 90^\circ$). Azimuth cut-off $L_{cut}=219$ m.

tortions of the wave patterns in the image. The nonlinearity grows, smearing out the SAR information of the shorter azimuthal waves. This is illustrated in Figure 2.3. The bimodal simulated wave spectrum (a) consists of a swell component with $H_s=2.5$ m, $L_p=585$ m propagating in the azimuth direction (identical as the one shown in Figure 2.2), with a windsea component propagating in the range direction ($\phi_p = 90^\circ$) with $H_s=3.0$ m and $L_p=205$ m. In this case $L_{cut}=219$ m, closer to the swell peak wavelength. Compared to Figure 2.2, the azimuth cut-off effect becomes more significant, caused by the steep windsea — naturally, not observed in Figures 2.2(b) and 2.3(b) computed with the linear forward mapping. The differences are more marked between the linear and nonlinear image spectra and the linear inverted wave spectrum is expected to be, comparatively, more discrepant. However, the azimuth travelling swell peak is visible in both real parts of the SAR image spectra — Figure 2.3(b) and 2.3(c) — with the correct propagation direction indicated in 2.3(d). The range travelling windsea peak is not severely affected by the azimuth cut-off, and is also discernible in the image spectra. Its single peak is split in two — as commonly observed in SAR image spectra [2, 7] — because the Velocity Bunching MTF vanishes in the range direction.

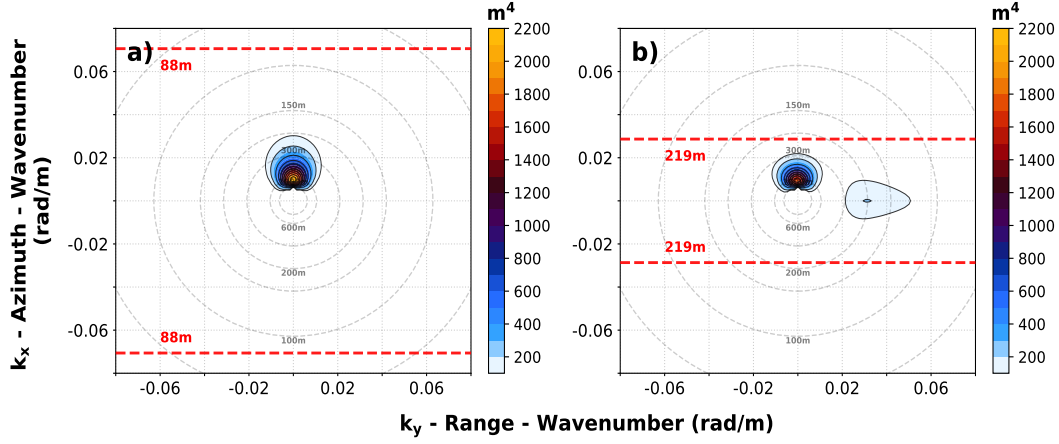


Figure 2.4: Retrieved wave spectra employing the LIM; (a) corresponding to the simulation depicted in Figure 2.2(a) and (b) corresponding to the simulation depicted in Figure 2.3(a). The peak wavelengths and directions are fairly well represented, apart from a reduction in \hat{H}_s .

The retrieved wave spectra employing the LIM to the complex SAR image cross spectra depicted in Figures 2.2 and Figure 2.3 are shown in Figure 2.4. In Figure 2.4(a) the unimodal, azimuth travelling swell component is well reproduced, retaining most of the simulated features of the input wave spectrum. A small reduction in the value of the retrieved significant wave height is also noticeable, from $H_s=2.50$ m to $\hat{H}_s=2.20$ m. The wave spectrum from the more challenging case presented in Figure 2.3 is also fairly well retrieved. The subestimation of the swell component propagating in the azimuthal direction is comparatively more pronounced, from $H_s=2.50$ m to $\hat{H}_s=1.61$ m. The windsea component is also attenuated, from the simulated 3.0 m to $\hat{H}_s=1.71$ m. The attenuation in \hat{H}_s employing the LIM depends on the propagation direction and on the relative position of the peak wavelength in respect to the azimuth cut-off, as will be discussed in the next chapters.

Capítulo 3

Nonlinearities in the Mapping Mechanism

The imaging mechanisms described by the RAR MTF's (Equation 2.7) can detect only waves propagating with a component in the range direction. The nonlinearities of the Hydrodynamic and Tilt modulations are small for the typical incidence angles of SAR satellites. Whereas the Velocity Bunching mechanism (Equation 2.8) is able to image waves traveling in the azimuthal direction and is also, generally, the dominant among all MTF's — with the exception of waves propagating purely in the range direction.

The nonlinear Velocity Bunching mechanism, caused by orbital motion Doppler shifts, produces displacements of the scattering elements. This results in the redistribution of the apparent backscattering density in the positive or negative azimuth direction, depending on the surface motion with respect to the satellite flight direction. These azimuthal displacements are sea state dependent and are also particularly relevant for high range to platform velocity ratios β , typical in spaceborne SAR systems. For small wave steepnesses the modulation can be assumed as linear. However, when the steepness increases, the Velocity Bunching mechanism becomes nonlinear and the azimuthal displacements increase correspondingly. When they become comparable with the wavelength, the components beyond a certain azimuthal wavenumber are not completely mapped.

The effects of strong nonlinearities in the SAR mapping are illustrated in Figure 3.1. The upper left panel shows a simulated bimodal wave spectrum with a range traveling swell with $H_s=2$ m and $L_p=455$ m and a steep windsea component propagating in azimuth direction with $H_s=3$ m and $L_p=205$ m. Also shown the real part of the cross spectrum obtained with the forward linear and nonlinear mappings (respectively b and c panels). The azimuth cut-off effect is evident in the nonlinear SAR image spectrum, with $L_{cut}=211$ m. The azimuthal windsea peak is located beyond the cut-off and therefore not visible in the nonlinear image spectrum. In the

linear image spectrum shown in Figure 3.1(b), on the other hand, the swell peak is dwarfed by the more energetic windsea peak.

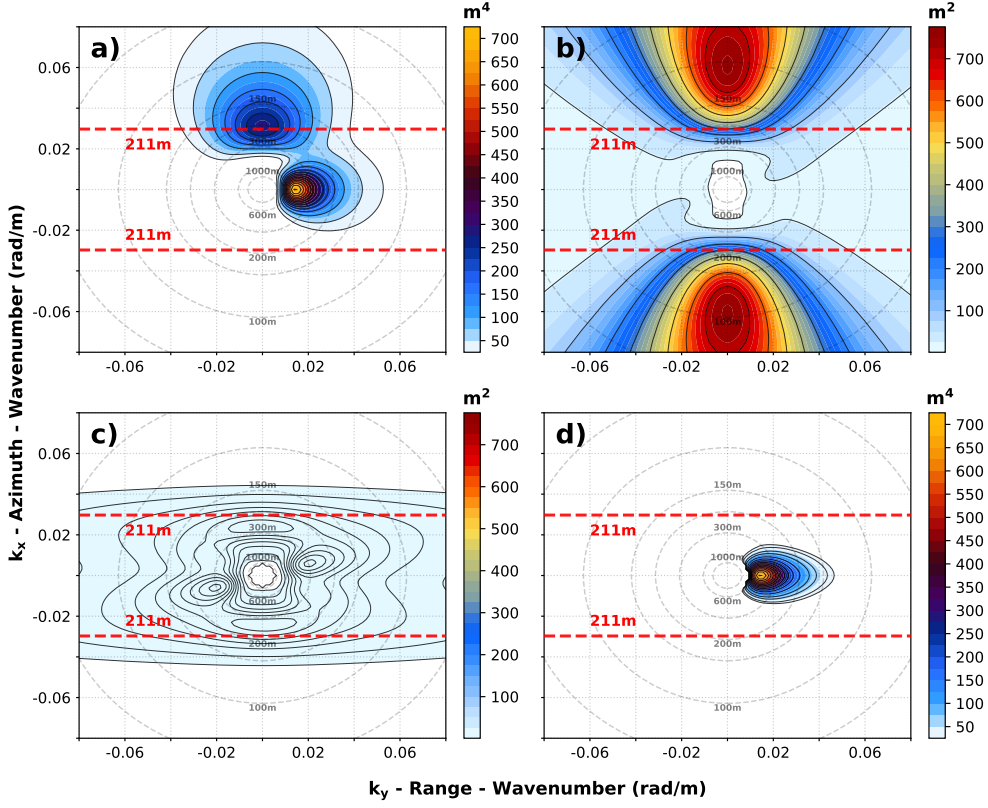


Figure 3.1: Ocean wave imaging mechanism using the simulator of complex image cross spectra. A simulated bimodal wave spectrum (a), with a swell propagating in the positive range direction ($H_s=2.0$ m, $L_p=455$ m and $\sigma = 20^\circ$) and a windsea component propagating in the azimuthal direction ($H_s=3.0$ m, $L_p=205$ m and $\sigma = 24^\circ$). The real part of its linear SAR cross spectrum is shown in (b), whilst (c) is the real part of the nonlinear image spectrum. In (d), the retrieved wave spectrum using the LIM. Azimuth cut-off $L_{cut}=211$ m.

Another distinction between the image spectra in Figures 3.1(b) and (c) is the two symmetrical ridges parallel to the range axis in low azimuthal wavenumbers, only present in the nonlinear spectrum. The azimuth cut-off generally lies within the windsea part of the spectrum. The energy contained in this region is transferred to low azimuthal wavenumbers because of the nonlinearities in the imaging process [6, 18] — observed as the two ridges parallel to the range axis in the nonlinear SAR image spectrum. The level of these symmetrical ridges is related to the windsea spectrum and can be employed to extract useful information about the high azimuthal wavenumber band [18, 29], even though the windsea peak itself is not visible in the image spectrum. In the linear forward mapping, the Fourier series expansion shown in Equation (2.9) is truncated and the first linear term is retained without the cut-off factor. Therefore, the linear approximation is, naturally, unable to account for the nonlinear effects in the mapping mechanism.

Figure 3.1(d) is the retrieved wave spectrum applying the LIM to the nonlinear

image spectrum shown in Figure 3.1(c). The range travelling swell is fairly represented, with good match with the simulated spectrum in terms of peak wavelength and direction. The already discussed reduction in \hat{H}_s is also observed, from 2.0 m to 1.82 m in the swell component. The windsea spectrum, located beyond the azimuth cut-off, is therefore not recovered.

Capítulo 4

Simulated Test Cases

Several cases were simulated to evaluate the wave spectrum retrieved from the LIM against the prescribed wave spectrum used as input to the simulator. As only the simulated SAR cross spectrum is used as input with no additional *a priori* information, the retrieved wave spectrum is restricted to the low wavenumber band. The full nonlinear forward relation is applied to a parametric JONSWAP wave spectrum mapping it onto a SAR cross spectrum, for a time lag τ of 0.33 second and 0.39 second — for both Sentinel-1 and Envisat configurations, respectively. Controlled experiments were designed to evaluate how changes in specific wave input parameters impact the simulated SAR cross spectrum — and subsequently its inversion — which allows, for instance, to investigate theoretical sea states conditions.

Nonlinear distortions degrade the spectral band beyond the azimuth cut-off, which has to be taken into account for the assessment of the LIM. Therefore a consistency test was performed on the retrieved spectra consisting of two conditions. Firstly, \hat{L}_p has to lie within ± 200 m of the value of L_p . And, additionally, \hat{H}_s has to be at least 20% of H_s — no restrictions were imposed on the retrieved peak direction. These threshold values were optimized against a subset of retrieved wave spectra after several iterations inspecting visually their shapes and main parameters. If both two conditions are not satisfied, the retrieved wave spectrum is considered unrelated to the input wave spectrum because of severe nonlinear distortions and is not considered as an acceptable retrieval.

The simulated unimodal spectra comprised combinations of H_s and L_p for three distinct propagation directions, for both Envisat and Sentinel-1, for a constant $\sigma = 20^\circ$. Figure 4.1 depicts those that passed the consistency test for azimuth, range and intermediate (between both directions) traveling waves, for Envisat. The azimuth cut-off, also shown, depends on propagation direction, satellite configuration, H_s and L_p — Equation 2.5. Similar plots, not shown, describe the relationship between L_p and L_{cut} for Sentinel-1 as well. The dashed line depicts when L_{cut} equals L_p , with values above it representing wave configurations whose azimuth cut-off is

higher than the peak wavelength. Nonlinear effects therefore are more significant the further away above the line, for waves with an azimuthal component. On the other hand, below the dashed line, an approximately linear mapping process is expected. Therefore the simulations encompass a broad range of steepnesses, for two different satellite configurations, and for three distinct propagation directions — azimuthal (0°), intermediate (45°) and range (90°).

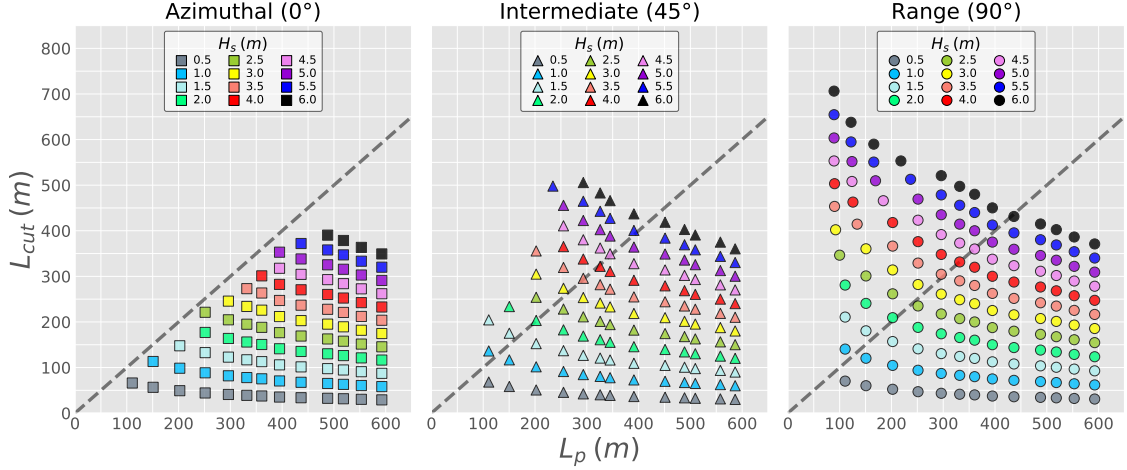


Figure 4.1: From left to right: relationship between L_p and L_{cut} for azimuth, intermediate and range travelling waves, assuming the Envisat configuration. The dashed line shows when L_p equals L_{cut} and can be think of a delimiter between nonlinear (above the line) and linear (below the line) SAR mapping of the wave component. The colors represent distinct values of H_s . For each combination of H_s and L_p a SAR cross spectrum was simulated employing the integral forward mapping relation. The three panels show the combinations in which the retrieved spectra passed the consistency test.

Figure 4.2 shows the relative error of \hat{H}_s , represented as

$$\mathcal{E}^{H_s} = \frac{\hat{H}_s - H_s}{H_s}.$$

Moreover, P_{cut} is the relative difference between \hat{L}_p and L_{cut} , in the form

$$P_{cut} = \frac{\hat{L}_p - L_{cut}}{\hat{L}_p}.$$

Envisat and Sentinel-1 were orbiting at different altitudes, therefore their parameter β differ and, consequently, L_{cut} and P_{cut} are also distinct in both satellites. The LIM underestimates the value of \hat{H}_s , whose magnitude depends on the propagation direction and on the relative position of the retrieved peak wavelength with respect to the azimuth cut-off. Naturally, waves propagating in the azimuthal direction or having a component in this direction are more severely attenuated the closer \hat{L}_p

approaches — and eventually overtakes — L_{cut} .

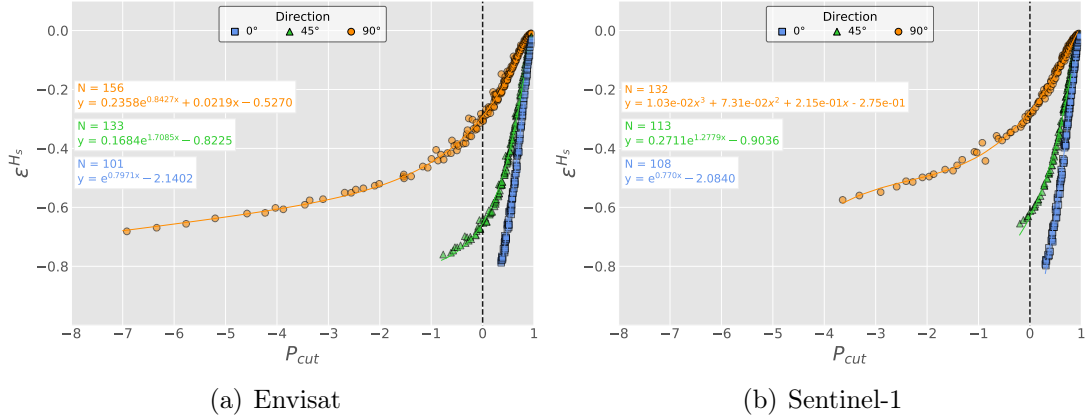


Figure 4.2: Relative error of \hat{H}_s for azimuthal (0° – blue square), intermediate (45° – green triangle) and range (90° – orange circle) directions — for Envisat (a) and for Sentinel-1 (b) configurations. The vertical axis is \mathcal{E}^{H_s} , the relative error between simulated and retrieved significant wave height. The negative sign in \mathcal{E}^{H_s} indicates underestimation. The horizontal axis is P_{cut} , the relative distance between \hat{L}_p and L_{cut} . The vertical dashed line shows when $\hat{L}_p = L_{cut}$. Negative values of P_{cut} indicate that \hat{L}_p is smaller than L_{cut} and nonlinear effects become relevant. Also shown the number of entries N and the best fit of the data.

Beyond the azimuth cut-off (hence for $P_{cut} < 0$), the spectrum is severely blurred and becomes rapidly unrecoverable the closer the waves are propagating to the azimuthal direction. Therefore, the number of \hat{H}_s (shown in the plots) is different for each direction and for each satellite. Range traveling waves, less affected by the azimuth cut-off, are only limited in high wavenumber by the range resolution which depends on the bandwidth of the radar [21]. However, the underestimation also increases as function of P_{cut} , reaching a limit of around 70% of H_s for Envisat. Waves propagating in the intermediate direction are reduced around 80% of H_s in the limit when \hat{L}_p is half the value of L_{cut} — for $P_{cut} \approx -1$. Similar behaviour is observed for Sentinel-1.

For positive values of P_{cut} , hence within a — roughly — linear part of the spectrum, \hat{H}_s is also mostly underestimated (Figure 4.2). When \hat{L}_p is four to five times larger than L_{cut} and hence $P_{cut} \rightarrow 1$, \hat{H}_s is close to H_s ($\mathcal{E}^{H_s} \rightarrow 0$) for the three considered directions and for both satellites. At this spectral region, quite away from the azimuth cut-off, the nonlinear effects are negligible and the LIM yields a nearly perfect retrieval — as illustrated in Figure 2.2. The underestimation becomes more significant the closer \hat{L}_p approaches L_{cut} , as exemplified in Figures 2.3 and 3.1. For range travelling waves, the underestimation when $P_{cut} = 0$ is around 30% of H_s for Envisat and Sentinel-1 configurations. For waves with an azimuthal component, even for positive values of P_{cut} , the underestimation can be as large as 80% of H_s . When \hat{L}_p is twice the value of L_{cut} ($P_{cut} = 0.5$), the underestimation can be as large

as 40% for azimuth and intermediate waves.

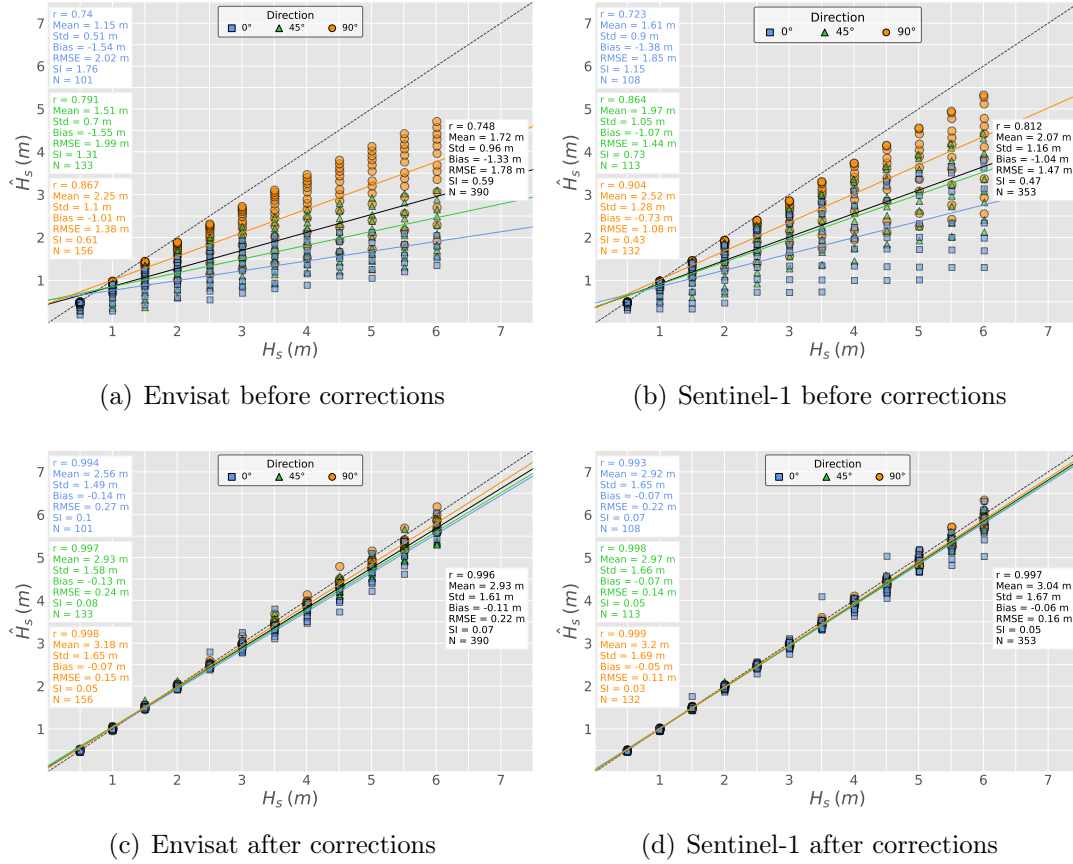


Figure 4.3: Scatter plots of retrieved versus simulated significant wave height, for Envisat (left column) and Sentinel-1 (right column) before (first row) and after (second row) the empirical corrections shown in Figure 4.2. For the three reference directions. Also shown the statistical parameters for each direction (on the left) and the whole data set (on the right).

Four strategies were evaluated to attempt to correct the underestimation of \hat{H}_s . The real part of the cross spectra computed with the nonlinear forward mapping relation have smaller magnitudes in relation to the yielded by the linear forward mapping, as shown for instance in panels b and c in Figures 2.3 and 3.1. Considering that, in theory, the linear inversion of a linear image spectrum yields the exact simulated wave spectrum, the ratio between the linear image spectrum and the nonlinear image spectrum can be used as a scale factor for the correction of \hat{H}_s . Therefore, the ratio between the maximum values of the real parts of both spectra were computed and applied to the simulated nonlinear image spectrum. Its linear inversion was subsequently computed, reducing significantly the underestimation of \hat{H}_s . In a similar fashion, but with poorer results, the second procedure employed the ratio between the mean values of the real parts of both spectra and was also implemented to correct the reduction in \hat{H}_s . The third approach was based on the semiempirical expression proposed by [33] relating significant wave height

to peak wavelength, cut-off and peak propagation direction. In this case, the underestimation was properly corrected for smaller values of significant wave height but, as described by the authors, their expression is not as effective for values greater than 3 m. More robust results, however, were obtained by the fourth strategy which employed the empirical regressions depicted in Figure 4.2 to correct the biases. The energy of the retrieved wave spectra was simply rescaled to compensate the underestimation of \hat{H}_s .

Scatter plots of retrieved and simulated significant wave height are shown in Figure 4.3, for both Envisat and Sentinel-1, before and after the corrections using the proposed empirical regressions shown in Figure 4.2. The underestimation of \hat{H}_s is evident in the first row, more accentuated for waves propagating in the pure azimuthal direction. Some statistical parameters are also shown in the plots, for each of the discussed reference directions and for the whole data set. Prior to the corrections, as a whole, \hat{H}_s for Envisat presented a Root Mean Square Error (RMSE) of 1.78 m, Scatter Index (SI) of 0.59, Pearson Correlation (r) of 0.75 and Bias of -1.33 m. The spread of the fitted values shown in Figure 4.2 is small, therefore as expected, the corrections are effective in improving \hat{H}_s — second row in Figure 4.3. The errors are drastically reduced, for both satellite configurations. The corrections are slightly less effective for larger values of H_s and also for the purely azimuthal waves, but overall the (after correction) \hat{H}_s have small values of Bias, RMSE and SI. This approach will be applied to Envisat data, as will be shown in the following chapter.

Likewise, \mathcal{E}^{L_p} is the relative error of \hat{L}_p :

$$\mathcal{E}^{L_p} = \frac{\hat{L}_p - L_p}{L_p}.$$

Top line in Figure 4.4 shows P_{cut} versus \mathcal{E}^{L_p} for the three reference directions and for Envisat (a) and Sentinel-1 (b). For range traveling waves, \hat{L}_p is identical to the simulated, for the whole range of P_{cut} considered and for both satellites. The LIM does not take into account, evidently, the nonlinearities of the Velocity Bunching mechanism, which are more pronounced in the azimuth direction. Waves propagating in — or with a component in — the azimuthal direction, are shifted into low azimuthal wavenumbers. The shift is more accentuated as P_{cut} decreases and for pure azimuthal waves, with the spectral peak moving towards longer wavelengths — the superestimation of \hat{L}_p can be of up to 60% (Sentinel-1) and 40% (Envisat) of L_p for azimuthal waves. As expected, the spectrum becomes gradually irretrievable when P_{cut} becomes negative. The regressions shown in Figure 4.4 (top line) were applied to the retrieved wave spectra, with the corrected \hat{L}_p depicted in the bottom line.

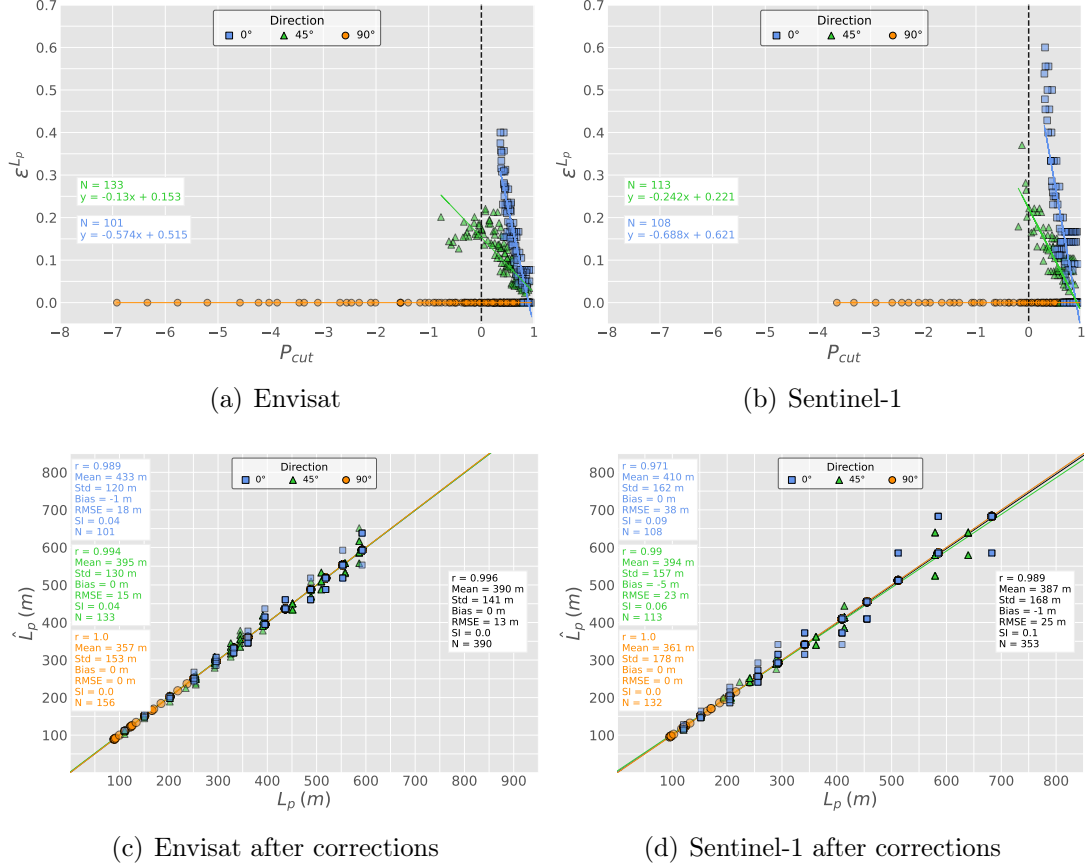


Figure 4.4: Top line: relative error of \hat{L}_p for azimuthal (0° – blue square), intermediate (45° – green triangle) and range (90° – orange circle) directions — for Envisat (a) and for Sentinel-1 (b) configurations. The horizontal axis is P_{cut} , the relative distance between \hat{L}_p and L_{cut} . The vertical dashed line shows when $\hat{L}_p = L_{cut}$. The vertical axis is \mathcal{E}^{L_p} and the positive sign indicates superestimation. Bottom line: values of \hat{L}_p after the empirical corrections depicted in the top line. Also shown the number of entries N and the best fit of the data.

The bias is nearly zero, with small values of SI and RMSE for both satellites.

The spectra were simulated in three distinct peak wave directions — azimuthal, range an intermediate. The absolute error of $\hat{\phi}_p$ is expressed as

$$\mathcal{E}^{\phi_p} = \min\{\gamma, 2 - \gamma\} \times 180,$$

where $\gamma = \frac{|\hat{\phi}_p - \phi_p|}{180}$. The retrieved and the simulated peak wave directions are shown in the top line in Figure 4.5, for Envisat (a) and Sentinel-1 (b). The nonlinearities cause a rotation of $\hat{\phi}_p$ into the range direction with respect to the simulated peak direction. Only waves propagating in the intermediate direction are rotated. As already discussed, range travelling waves are unaffected. On the other hand, the pure azimuthal waves do not experience any change in direction since the shift is along the azimuthal axis. The strongest deviations are observed around the cut-off

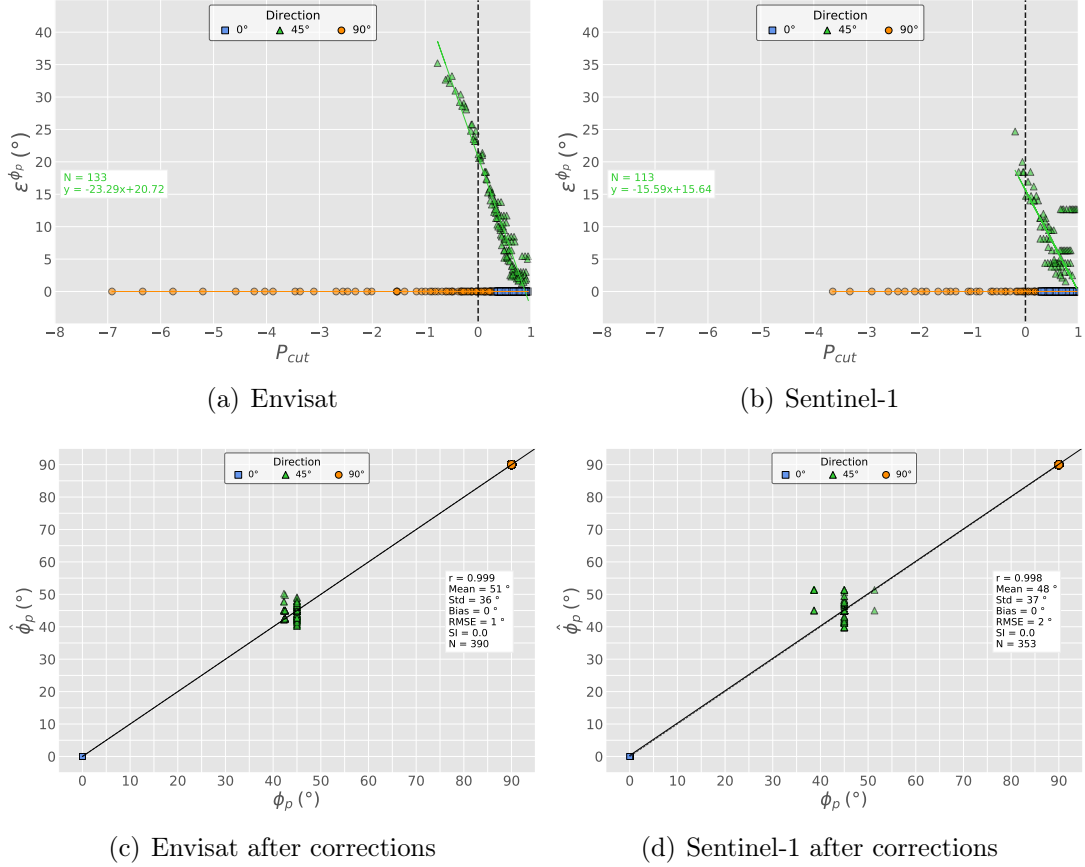


Figure 4.5: Top line: absolute error of $\hat{\phi}_p$ for azimuthal (0° – blue square), intermediate (45° – green triangle) and range (90° – orange circle) directions — for Envisat (a) and for Sentinel-1 (b) configurations. The horizontal axis is P_{cut} . The vertical dashed line shows when $\hat{L}_p = L_{cut}$. The vertical axis is \mathcal{E}^{ϕ_p} , the absolute difference between retrieved and simulated ϕ_p . Positive values of \mathcal{E}^{ϕ_p} indicate that the waves are rotating into the range direction with respect to the simulated direction. Only waves propagating in the intermediate direction are affected. Bottom line: values of $\hat{\phi}_p$ after the empirical corrections depicted in the top line. Also shown the number of entries N and the best fit of the data.

wavelength, with a maximum value of 35° for Envisat and 25° for Sentinel-1. The regressions to correct $\hat{\phi}_p$ in the intermediate direction, shown in the top line, were applied to rotate the retrieved wave spectrum. The corrections of $\hat{\phi}_p$, shown in the bottom line in Figure 4.5, are effective, resulting in zero bias and small values of RMSE and SI.

The underestimations (of \hat{H}_s) and superestimations (of \hat{L}_p and $\hat{\phi}_p$) are expected to be rigorously dependent on the satellite configuration, propagation direction and P_{cut} . Hence, the regressions presented in Figures 4.2, 4.4 and 4.5 can be used as lookup tables to correct biases. Wave spectra retrieved with the LIM using Envisat ASAR Cross Spectra are discussed in the next chapter.

Capítulo 5

Envisat ASAR Level 1 Cross Spectra (WVS)

The Envisat ASAR Wave Mode imagettes — approximately 5 km along-track and up to 10 km across-track — were routinely acquired at 100 km intervals during the satellite 10 years of operation. A segment of ground track 0383 used in our analysis, over the Eastern Pacific Ocean, is shown in Figure 5.1. Multi-modal wave spectra are common in the region, with significant wave height varying between 1.38 m and 5.02 m along this segment. The Level 1 cross-spectra (WVS), downloadable from ESA’s Earth Online website, were used as input for the LIM to retrieve ocean wave spectra. Only images covering depths greater than 1000 m were retained, with a total of 101 ASAR WVS cross spectra. No limit on latitude, because of ice cover, was imposed although some of the most southern did not pass the homogeneity test discussed below. Additionally, the cases of $\hat{H}_s < 0.1$ m were discarded.

The retrieval of a wave spectrum employing the LIM takes place, briefly, in two steps. The signal processing module of the complex images constitutes the first step. Low frequency signatures, unrelated to wind waves, are filtered out. Inhomogeneities in ocean SAR images are frequent under low wind conditions but could also be related to oceanic fronts, internal waves, sea ice, oil slicks and rain cells among other phenomena [see for instance homogeneity tests discussed in 25]. The filtering technique is centered around the lowest wavenumber bins, removing therefore the non-wave features. Additionally, the high frequency band — beyond the azimuth cut-off — is heavily distorted. This part is also filtered, using the estimated cut-off wavelength from the product metadata.

In the second step, the real part of the filtered cross spectrum is partitioned — as described in [30] — breaking down a multi-modal image spectrum into a limited number of unimodal spectra with its corresponding counterpart in the imaginary part. The LIM is applied to each partition, yielding the corresponding wave spectrum. The regressions computed in chapter 4 for H_s , L_p and ϕ_p are employed to

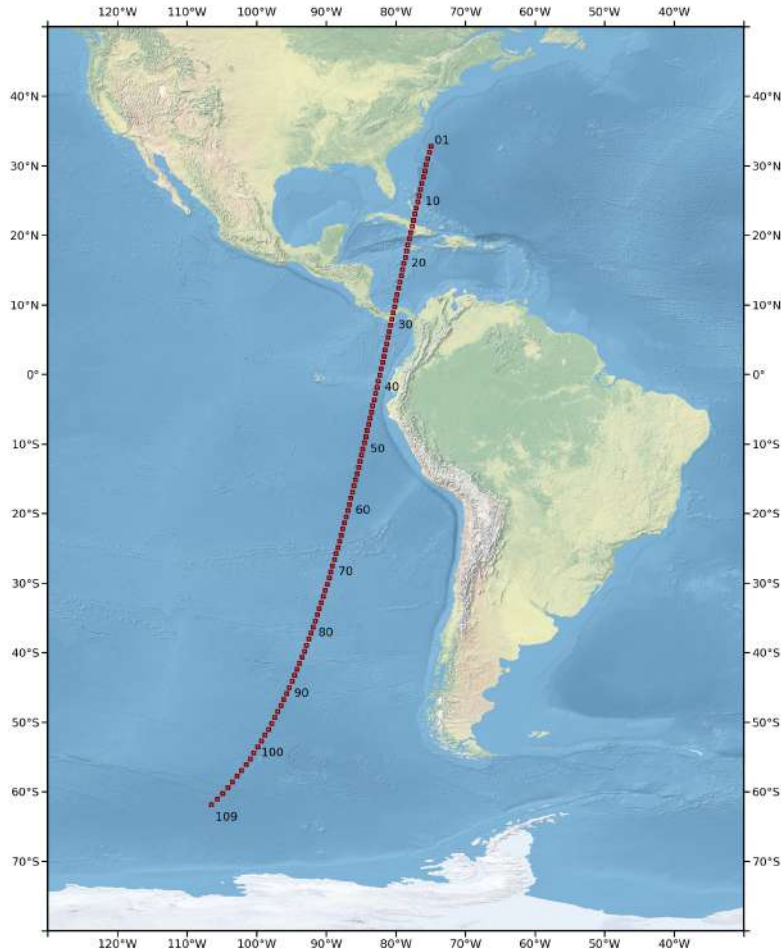


Figure 5.1: Segment of Envisat ground track 0383 on 18 January 2009 around 15:09 UTC, with 109 spectra. The figures describe their spatial distribution.

correct the retrieved wave partitions — with rotations in direction and shifts in wavelength. The spectrum is rescaled — with no changes in its shape — to attain the expected increase in \hat{H}_s . Finally, each partition is linearly summed, building up the retrieved directional wave spectrum.

The retrieval method to generate the ESA L2 WWV product is based on the assumption that the measured SAR cross spectrum can be approximated as the combination of a non-linear and a quasi-linear part, related mainly — respectively — with the windsea and swell contributions [3]. Employing an estimated wind field, generally from a numerical model, the windsea spectrum is computed with its stage of development determined based on a minimization function between the observed and simulated image spectra. Using the nonlinear forward mapping relation, the windsea image spectrum is calculated and subsequently subtracted from the measured spectrum — the residual SAR spectrum is assumed to be only related to the quasi-linear contribution from the swell components. The Level 2 WWV product are provided on a log-polar grid with 24 wavelengths and 36 directions. The WWV wave spectra are limited by the azimuth cut-off wavelength and hence the evaluation

of their derived parameters are generally restricted to the low wavenumber band.

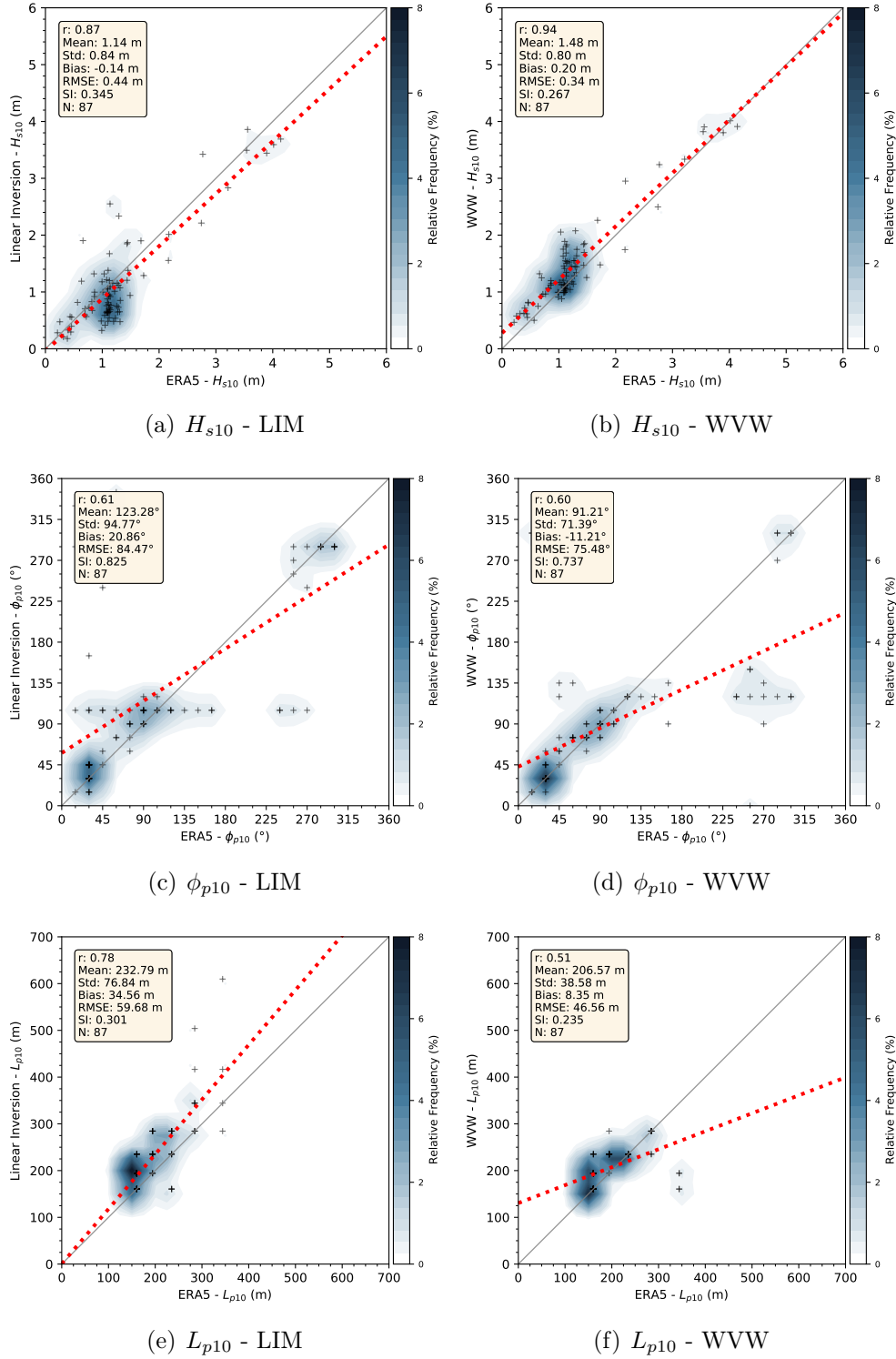


Figure 5.2: Scatterplots of, respectively, H_{s10} (a and b), ϕ_{p10} (c and d) and L_{p10} (e and f). For the ERA5 against the LIM (left column) and ERA5 against WWV (right column). Also shown the Pearson correlation (r), Mean, Standard Deviation (Std), Bias, Root Mean Square Error (RMSE), Scatter Index (SI) and number of entries (N) — 87 cases passed the homogeneity tests.

Because of the limitations in the azimuthal high wavenumber part of the

wave spectrum, a meaningful statistical analysis has to be limited in frequency space. The retrieved wave spectra using the LIM were evaluated against ERA5 spectra from the ECMWF atmospheric reanalysis — ERA5, downloadable from cds.climate.copernicus.eu. The high spatial and temporal resolution of the ERA5 globally distributed database contains hourly realizations at 40 km for wave spectra with 24 directions and 30 frequencies. The collocation was performed to the Envisat Wave Mode imagettes shown in Figure 5.1 using the nearest model grid point and synoptic time, which means less than 17 km and less than 29 minutes. Additionally, WVW spectra were also compared with ERA5 spectra for performance evaluation of the retrieval methods. Scatterplots of the SAR retrievals with the LIM against ERA5 (left column) and of WVW spectra against ERA5 (right column) are presented in Figure 5.2.

Significant wave height, for waves with periods longer than 10 s (which corresponds to lengths longer than 156 m in deep water), is computed as

$$H_{s10} = 4 \sqrt{\int \int_{<10s^{-1}} F(f, \theta) df d\theta},$$

where $F(f, \theta)$ is the frequency-direction wave spectrum — SAR-inverted wave spectra were converted from wavenumber-direction $F(kx, ky)$. Despite the procedure to rescale the spectrum using the regression presented in chapter 4, the retrieved H_{s10} is still underestimated with a negative bias of approximately 14 cm — Figure 5.2(a). The RMSE is 0.44 m for a Pearson correlation of $r = 0.87$ and SI of 0.34. The results of WVW for H_{s10} (Figure 5.2(b)) are more accurate, with a higher positive bias of 20 cm but smaller RMSE and SI of, respectively, 0.34 m and 0.27. H_{s10} is the wave parameter better retrieved in both methods, but the WVW results are very satisfying, having small statistical errors.

Likewise, peak direction, for waves with periods longer than 10 s (ϕ_{p10}) is shown in Figures 5.2(c) and (d). SAR-inverted wave spectra, retrieved with both methods have statistically similar results, with WVW showing slightly smaller errors. Both procedures do not rely on any *a priori* wave information to resolve the directional ambiguity, employing the phase information to determine the correct propagation direction in the cross-spectral analysis. In the ESA retrieval method, if the signal-to-noise ratio (SNR) of the spectrum is below a given threshold, the ambiguity is not removed [3, 9]. The spectrum is kept unchanged with the symmetrical peaks retained in the retrieved wave spectrum. The parameter ϕ_{p10} , integrated over frequency, therefore can not pinpoint such cases of unresolved ambiguity.

Figures 5.2(e) and (f) depict the peak wavelength for waves with periods longer than 10 s, $L_{p10} = \frac{g}{2\pi f_{p10}^2}$ where g is the gravitational acceleration and the peak fre-

quency for waves with periods longer than 10 s is f_{p10} . The WWV results presented smaller RMSE, bias and SI — the LIM showed a better correlation. The already discussed superestimation of L_{p10} retrieved with the LIM is also clear with the Envisat ASAR data, with a positive bias of 34.56 m after applying the corrections. The peak wavelength from the WWV spectra presented a smaller superestimation of 8.35 m.



Figure 5.3: The parameter Ω (Equation 5.1) is a matrix square error normalized with the square of the reference wave spectrum (ERA5), computed along the ground track shown in Figure 5.1. Small values of Ω indicate close proximity between spectra. For wave spectra retrieved with the LIM (green diamond) and with the ESA procedure (WWV, pink circle). Also shown, as red circles, the cases where the directional ambiguity was not properly resolved (WWV - Amb) — Equation 5.2.

Despite the overall good results of the SAR wave parameters computed with both methods, a closer analysis of the spectral shape shows some discrepancies with the ERA5 directional spectrum. A metric for evaluation of the agreement between directional spectra is hence proposed as

$$\Omega = \frac{\int \int [F_{eva}(f, \theta) - F_{ref}(f, \theta)]^2 df d\theta}{\int \int [F_{ref}(f, \theta)]^2 df d\theta}, \quad (5.1)$$

where $F_{ref}(f, \theta)$ is the reference — ERA5 spectrum — and $F_{eva}(f, \theta)$ is the evaluated spectrum — retrieved from the LIM or the WWV wave mode. The dimensionless parameter Ω is a matrix square error normalized with the square of the reference spectrum, being zero for identical spectra — its value increases as their differences grow. In the following analysis, we are considering for evaluation of Ω the whole $F(f, \theta)$ spectrum, without imposing any high frequency band limitation. Therefore, discrepancies between the ERA5 spectra and the SAR retrieved wave spectra are expected, specially in high frequency. Figure 5.3 shows the values of Ω along the

ground track, for the wave spectra retrieved with the LIM and also for ESA WVW wave mode spectra. Disregarding anomalous results outside the range $0 < \Omega < 6$, the shape of the retrieved spectra using the LIM is closer to the ERA5 spectra, with an average value of $\Omega = 1.13$. The shape of the WVW spectra is less similar, with an average value of $\Omega = 1.33$. Along the segment 40–80, characterized by unimodal spectra (not shown here) propagating in an intermediate direction, the results of the WVW spectra are closer to ERA5. The LIM along most of this segment presented an additional component, not present in the ERA5 spectra. This same component appeared in the WVW spectra in images 49, 50 and 51, when Ω increases. This might be related to noise that the ESA retrieval dealt better with its filtering.

The procedure to resolve the directional ambiguity in the ESA retrievals seems to be particularly sensitive to low SNR spectra. In such cases, both ambiguous peaks are kept in the retrieved directional wave spectra and a flag of low confidence in the inversion is attached to the data. An additional metric, analogous to Ω , is therefore employed to indicate when the directional ambiguity is not removed, in the form

$$\Omega_{amb} = \frac{\int \int [F_{eva(0,180)}(f, \theta) - F_{eva(180,360)}(f, \theta)]^2 df d\theta}{\int \int [F_{eva(0,360)}(f, \theta)]^2 df d\theta}. \quad (5.2)$$

The subindexes (0, 180) and (180, 360) represent a splitting of $F(f, \theta)$ in two halves with respect to the directional distribution, to search for ambiguities between them. In the denominator, the norm of the full, complete spectrum is considered — (0, 360). A threshold limit of $\Omega_{amb} < 0.35$ is fixed, which was optimized after manual inspection and validated against a subset of spectra, indicating that the ambiguous peaks are both present in the retrieved wave spectrum. For WVW spectra, 25 presented Ω_{amb} below the limit, which is 29% of the 87 cases considered — shown as red circles in Figure 5.3. The LIM is less sensitive to low SNR and the directional ambiguity was removed in all WVS cross spectra here considered — however, in a few cases, the LIM selected erroneously the unambiguous spectral peak. The presence of the ambiguous peaks in the WVW spectra caused their shape to drift apart from the ERA5 reference and a large amount of such cases severely penalized the mean value of Ω .

Capítulo 6

Summary and Conclusions

We have demonstrated the potential of the LIM to retrieve directional wave spectra from complex SAR cross spectra. The method does not require any additional external information as input, as is commonly the case with the known wave spectra retrieval schemes. Being linear, it is naturally a limited representation of the process, which is strongly nonlinear in the high azimuthal wavenumber band beyond the cut-off. We have presented regressions, employing a simulator of SAR cross spectra, to correct biases while retrieving wave spectra using the LIM. As the nonlinearities are dependent on satellite configuration and on the relative position of the peak wave spectrum in relation to the azimuth cut-off, it is possible to quantify these nonlinearities through numerical simulations. We have simulated SAR cross spectra using the full, nonlinear, forward mapping and compared the linearly retrieved wave spectra against the wave spectra used as input for the simulations. The discrepancies between simulated and retrieved wave spectra in terms of significant wave height, peak wave direction and peak wavelength were assumed to be caused mainly by the non inclusion of the nonlinear terms.

For the simulated cases, the LIM underestimates \hat{H}_s and, as well, superestimates \hat{L}_p and $\hat{\phi}_p$. For wave components with \hat{L}_p four to five times larger than the azimuth cut-off (L_{cut}) — for any of the three simulated directions: azimuthal, range and intermediate — the LIM yielded the nearly exact simulated spectra. The nonlinearities become gradually more relevant, for waves with an azimuthal component, when \hat{L}_p approaches L_{cut} — the spectrum comes to be rapidly irretrievable because of strong nonlinearities. The reduction in \hat{H}_s can be of up to 80% of the simulated values and the increase in \hat{L}_p of up to 40% (for Envisat), with $\hat{\phi}_p$ rotating towards the range direction with respect to the simulated direction. Waves propagating purely in the range direction, on the other hand, are unaffected by the azimuth cut-off, experiencing no variations in \hat{L}_p and $\hat{\phi}_p$ — although \hat{H}_s is also reduced, but at a smaller rate.

The nonlinearities, therefore, are responsible for a severe reduction in \hat{H}_s , regardless of wave propagation direction. Several methods were tested to correct this underestimation. However, the best results were obtained employing the regressions fitting the relative error between simulated and retrieved significant wave height versus the relative distance between \hat{L}_p and L_{cut} , depicted in Figure 4.2 — the subestimation of \hat{H}_s was nearly eliminated in the simulated experiments. Similarly, regressions for L_p and ϕ_p were also computed. Our simulated results of H_s , L_p and ϕ_p with respective regressions shown in Figures 4.2, 4.4 and 4.5, hence, can be employed as lookup tables for the LIM to correct biases associated with nonlinearities in the imaging mechanisms.

The LIM was validated using WVS Level 1 cross spectra from an Envisat ground track. The spectra were rotated, shifted and rescaled but keeping its original shape — applying the empirical corrections of H_s , L_p and ϕ_p . The linearly retrieved wave spectra were validated against the ERA5 reanalysis and compared to the results of WVW spectra. The preliminary results are encouraging. The parameters retrieved with the LIM show similar values when compared with the WVW spectra, although with slightly larger values of RMSE and SI. The shape of the spectra retrieved with the LIM presented, however, better similarity with the ERA5 wave spectra. The ESA methodology to retrieve the WVW wave spectra is apparently more sensitive to low signal-to-noise ratio image spectra, hindering its disambiguation. In around one in three WVW spectra the ambiguous propagation direction was not solved correctly with both peaks retained, which causes distortions of the spectral shape and dissimilarities with the wave model spectra.

The LIM, therefore, is — *per se* — an efficient and computationally cheap method to yield a very close approximation of the directional wave spectrum. It could be employed as first guess to more computer demanding retrieval schemes, with the advantage that requires no *a priori* information from wave or meteorological models. Moreover, could be also used to determine more efficiently the correct unambiguous propagation direction of the ESA distributed WVW spectra.

More importantly, it has the potential to be used as a self-contained and accurate SAR retrieval scheme. The regressions used to correct the retrieved Envisat ASAR wave spectrum using the LIM were based on simulations that did not include image noise, the so-called speckle. Speckle adds a white noise floor on the SAR image spectrum upon which the aimed wave spectrum resides, therefore impacting the retrieval process. More sophisticated approaches, for instance using neural networks and deep learning, could be used to generate more realistic empirical corrections. The LIM hence could be applied to real SAR images and the retrieved wave spectrum compared to collocated directional buoy spectra. These more robust regressions could be employed to rotate, shift and rescale the retrieved wave spectra — as

here demonstrated with the speckle noise free simulations. The LIM is, therefore, a comparatively simple and powerful method to retrieve SAR directional wave spectra.

Referências Bibliográficas

- [1] BAO, M., ALPERS, W., 1998, “On the cross spectrum between individual-look Synthetic Aperture Radar images of ocean waves”, *IEEE Transactions on Geoscience and Remote Sensing*, v. 36, n. 3 (May), pp. 922–932. ISSN: 0196-2892. doi: 10.1109/36.673683.
- [2] BRÜNING, C., ALPERS, W., HASSELMANN, K., 1990, “Monte-Carlo simulation studies of the nonlinear imaging of a two dimensional surface wave field by a synthetic aperture radar”, *International Journal of Remote Sensing*, v. 11, n. 10, pp. 1695–1727. doi: 10.1080/01431169008955125. Disponível em: <<https://doi.org/10.1080/01431169008955125>>.
- [3] CHAPRON, B., JOHNSEN, H., GARELLO, R., 2001, “Wave and wind retrieval from SAR images of the ocean”, *Annales des Télécommunications*, v. 56 (11), pp. 682–699. doi: 10.1007/BF02995562.
- [4] COLLARD, F., ARDHUIN, F., CHAPRON, B., 2009, “Monitoring and analysis of ocean swell fields from space: New methods for routine observations”, *Journal of Geophysical Research: Oceans*, v. 114, n. C7. doi: <https://doi.org/10.1029/2008JC005215>. Disponível em: <<https://agupubs.onlinelibrary.wiley.com/doi/abs/10.1029/2008JC005215>>.
- [5] ENGEN, G., JOHNSEN, H., 1995, “SAR-ocean wave inversion using image cross spectra”, *IEEE transactions on geoscience and remote sensing*, v. 33, n. 4, pp. 1047–1056.
- [6] HASSELMANN, K., RANEY, R. K., PLANT, W. J., et al., 1985, “Theory of Synthetic Aperture Radar ocean imaging: A MARSEN view”, *Journal of Geophysical Research: Oceans*, v. 90, n. C3, pp. 4659–4686. doi: 10.1029/JC090iC03p04659. Disponível em: <<https://agupubs.onlinelibrary.wiley.com/doi/abs/10.1029/JC090iC03p04659>>.
- [7] HASSELMANN, K., HASSELMANN, S., 1991, “On the nonlinear mapping of an ocean wave spectrum into a Synthetic Aperture Radar image spectrum

and its inversion”, *Journal of Geophysical Research: Oceans*, v. 96, n. C6, pp. 10713–10729.

- [8] HASSELMANN, S., BRÜNING, C., HASSELMANN, K., et al., 1996, “An improved algorithm for the retrieval of ocean wave spectra from Synthetic Aperture Radar image spectra”, *Journal of Geophysical Research: Oceans*, v. 101, n. C7, pp. 16615–16629. doi: 10.1029/96JC00798. Disponível em: <<https://agupubs.onlinelibrary.wiley.com/doi/abs/10.1029/96JC00798>>.
- [9] JOHNSEN, H., ENGEN, G., COLLARD, F., et al., 2006, *Envisat ASAR Level 2 Wave Mode Product Algorithm Specification–Software Requirements Document*. Relatório Técnico IT650/1-01, NORUT.
- [10] KERBAOL, V., CHAPRON, B., VACHON, P. W., 1998, “Analysis of ERS-1/2 Synthetic Aperture Radar wave mode imagettes”, *Journal of Geophysical Research: Oceans*, v. 103, n. C4, pp. 7833–7846. doi: <https://doi.org/10.1029/97JC01579>. Disponível em: <<https://agupubs.onlinelibrary.wiley.com/doi/abs/10.1029/97JC01579>>.
- [11] KROGSTAD, H. E., SAMSET, O., VACHON, P. W., 1994, “Generalizations of the non-linear ocean-SAR transform and a simplified SAR inversion algorithm”, *Atmosphere-Ocean*, v. 32, n. 1, pp. 61–82. doi: 10.1080/07055900.1994.9649490. Disponível em: <<https://doi.org/10.1080/07055900.1994.9649490>>.
- [12] LEHNER, S., SCHULZ-STELLENFLETH, J., SCHATTLER, B., et al., 2000, “Wind and wave measurements using complex ERS-2 SAR wave mode data”, *IEEE Transactions on Geoscience and Remote Sensing*, v. 38, n. 5, pp. 2246–2257. doi: 10.1109/36.868882.
- [13] LI, H., STOPA, J., MOUCHE, A., et al., 2021, “Assessment of ocean wave spectrum using global Envisat/ASAR data and hindcast simulation”, *Remote Sensing of Environment*, v. 264, pp. 112614. ISSN: 0034-4257. doi: <https://doi.org/10.1016/j.rse.2021.112614>. Disponível em: <<https://www.sciencedirect.com/science/article/pii/S0034425721003345>>.
- [14] LI, X.-M., HUANG, B., 2020, “A global sea state dataset from spaceborne Synthetic Aperture Radar wave mode data”, *Scientific data*, v. 7, n. 1, pp. 1–12.
- [15] LI, X.-M., LEHNER, S., BRUNS, T., 2011, “Ocean Wave Integral Parameter Measurements Using Envisat ASAR Wave Mode Data”, *IEEE Transac-*

- tions on Geoscience and Remote Sensing*, v. 49, n. 1, pp. 155–174. doi: 10.1109/TGRS.2010.2052364.
- [16] LYZENGA, D. R., 1986, “Numerical Simulation of Synthetic Aperture Radar Image Spectra for Ocean Waves”, *IEEE Transactions on Geoscience and Remote Sensing*, v. GE-24, n. 6, pp. 863–872. doi: 10.1109/TGRS.1986.289701.
- [17] MASSEL, S. R., 2017, *Ocean Surface Waves*. 3rd ed. , WORLD SCIENTIFIC. doi: 10.1142/10666. Disponível em: <<https://www.worldscientific.com/doi/abs/10.1142/10666>>.
- [18] MASTENBROEK, C., DE VALK, C. F., 2000, “A semiparametric algorithm to retrieve ocean wave spectra from Synthetic Aperture Radar”, *Journal of Geophysical Research: Oceans*, v. 105, n. C2, pp. 3497–3516. doi: <https://doi.org/10.1029/1999JC900282>. Disponível em: <<https://agupubs.onlinelibrary.wiley.com/doi/abs/10.1029/1999JC900282>>.
- [19] PORTILLA-YANDÚN, J., VALLADARES, C., VIOLANTE-CARVALHO, N., 2019, “A Hybrid Physical-Statistical Algorithm for SAR Wave Spectra Quality Assessment”, *IEEE Journal of Selected Topics in Applied Earth Observations and Remote Sensing*, v. 12, n. 10, pp. 3943–3948. doi: 10.1109/JSTARS.2019.2944115.
- [20] QUACH, B., GLASER, Y., STOPA, J., et al., 2021, “Deep Learning for Predicting Significant Wave Height From Synthetic Aperture Radar”, *IEEE Transactions on Geoscience and Remote Sensing*, v. 59, n. 3, pp. 1859–1867. doi: 10.1109/TGRS.2020.3003839.
- [21] ROBINSON, I., 2004, *Measuring the oceans from space: the principles and methods of satellite oceanography*. Springer/Praxis Publishing. Disponível em: <<https://eprints.soton.ac.uk/9866/>>.
- [22] ROMEISER, R., GRABER, H., CARUSO, M., et al., 2015, “A New Approach to Ocean Wave Parameter Estimates From C-Band ScanSAR Images”, *IEEE Transactions on Geoscience and Remote Sensing*, v. 53, n. 3, pp. 1320–1345. doi: 10.1109/TGRS.2014.2337663.
- [23] SANTOS, F. M., SANTOS, A. L., VIOLANTE-CARVALHO, N., et al., 2021, “A simulator of Synthetic Aperture Radar (SAR) image spectra: the applications on oceanswell waves”, *International Journal of Remote Sensing*, v. 42, n. 8, pp. 2981–3001. doi: 10.1080/01431161.2020.1847352. Disponível em: <<https://doi.org/10.1080/01431161.2020.1847352>>.

- [24] SCHULZ-STELLENFLETH, J., LEHNER, S., 2005, “A noise model for estimated Synthetic Aperture Radar look cross spectra acquired over the ocean”, *IEEE Transactions on Geoscience and Remote Sensing*, v. 43, n. 7 (July), pp. 1443–1452. ISSN: 0196-2892. doi: 10.1109/TGRS.2005.846871.
- [25] SCHULZ-STELLENFLETH, J., LEHNER, S., 2004, “Measurement of 2-D sea surface elevation fields using complex synthetic aperture radar data”, *IEEE Transactions on Geoscience and Remote Sensing*, v. 42, n. 6, pp. 1149–1160. doi: 10.1109/TGRS.2004.826811.
- [26] SCHULZ-STELLENFLETH, J., KÖNIG, T., LEHNER, S., 2007, “An empirical approach for the retrieval of integral ocean wave parameters from synthetic aperture radar data”, *Journal of Geophysical Research: Oceans*, v. 112, n. C3. doi: <https://doi.org/10.1029/2006JC003970>. Disponível em: <<https://agupubs.onlinelibrary.wiley.com/doi/abs/10.1029/2006JC003970>>.
- [27] SCHULZ-STELLENFLETH, J., 2003, *Ocean wave measurements using complex Synthetic Aperture Radar data*. Tese de Doutorado, Universität Hamburg, Hamburg.
- [28] STOPA, J. E., MOUCHE, A., 2017, “Significant wave heights from Sentinel-1 SAR: Validation and applications”, *Journal of Geophysical Research: Oceans*, v. 122, n. 3, pp. 1827–1848. doi: 10.1002/2016JC012364. Disponível em: <<https://agupubs.onlinelibrary.wiley.com/doi/abs/10.1002/2016JC012364>>.
- [29] STOPA, J. E., ARDHUIN, F., CHAPRON, B., et al., 2015, “Estimating wave orbital velocity through the azimuth cutoff from space-borne satellites”, *Journal of Geophysical Research: Oceans*, v. 120, n. 11, pp. 7616–7634. doi: 10.1002/2015JC011275. Disponível em: <<https://agupubs.onlinelibrary.wiley.com/doi/abs/10.1002/2015JC011275>>.
- [30] VIOLANTE-CARVALHO, N., ROBINSON, I. S., SCHULZ-STELLENFLETH, J., 2005, “Assessment of ERS Synthetic Aperture Radar wave spectra retrieved from the Max-Planck-Institut (MPI) scheme through intercomparisons of 1 year of directional buoy measurements”, *Journal of Geophysical Research: Oceans*, v. 110, n. C7. doi: <https://doi.org/10.1029/2004JC002382>. Disponível em: <<https://agupubs.onlinelibrary.wiley.com/doi/abs/10.1029/2004JC002382>>.
- [31] VIOLANTE-CARVALHO, N., ROBINSON, I. S., 2004, “Comparison of the two-dimensional directional wave spectra retrieved from spa-

ceborne Synthetic Aperture Radar images using the MPI scheme against directional buoy measurements”, *Scientia Marina*, v. 68, n. 3 (Sep.), pp. 317–330. doi: 10.3989/scimar.2004.68n3317. Disponível em: <<https://scientiamarina.revistas.csic.es/index.php/scientiamarina/article/view/376>>.

- [32] VIOLANTE-CARVALHO, N., ROBINSON, I., GOMMENGINGER, C., et al., 2012, “The effect of the spatially inhomogeneous wind field on the wave spectra employing an ERS-2 SAR PRI image”, *Continental Shelf Research*, v. 36, pp. 1–7. ISSN: 0278-4343. doi: <https://doi.org/10.1016/j.csr.2011.12.006>. Disponível em: <<https://www.sciencedirect.com/science/article/pii/S0278434311003773>>.
- [33] WANG, H., JIANHUA, Z., YANG, J., et al., 2012, “A semiempirical algorithm for SAR wave height retrieval and its validation using Envisat ASAR wave mode data”, *Acta Oceanologica Sinica*, v. 31 (05). doi: 10.1007/s13131-012-0206-z.
- [34] WANG, H., ZHU, J., YANG, J., 2014, “Error Analysis on ESA’s Envisat ASAR Wave Mode Significant Wave Height Retrievals Using Triple Collocation Model”, *Remote Sensing*, v. 6, n. 12, pp. 12217–12233. ISSN: 2072-4292. doi: 10.3390/rs61212217. Disponível em: <<https://www.mdpi.com/2072-4292/6/12/12217>>.
- [35] YANG, J., WANG, H., XIAO, Q., et al., 2007, “Simulation of SAR image cross spectra from mixed ocean wave”. In: *2007 IEEE International Geoscience and Remote Sensing Symposium*, pp. 952–954. doi: 10.1109/IGARSS.2007.4422956.